A μSR AND NMR STUDY OF QUANTUM TUNNELING OF THE MAGNETIZATION IN HIGH SPIN MOLECULES

ZAHER SALMAN

A μSR AND NMR STUDY OF QUANTUM TUNNELING OF THE MAGNETIZATION IN HIGH SPIN MOLECULES

RESEARCH THESIS

SUBMITTED IN PARTIAL FULFILLMENT OF THE

REQUIREMENTS FOR THE DEGREE OF

DOCTOR OF PHILOSOPHY

ZAHER SALMAN

SUBMITTED TO THE SENATE OF THE TECHNION — ISRAEL INSTITUTE OF TECHNOLOGY

SIVAN, 5762 HAIFA MAY, 2002

THIS RESEARCH THESIS WAS SUPERVISED BY DR. AMIT KEREN UNDER THE AUSPICES OF THE PHYSICS DEPARTMENT

ACKNOWLEDGMENT

I thank Dr. Amit Keren for his fruitful guidance during all stages of research, and for a great working atmosphere. Special gratitude to Prof. Philippe Mendels for instructive talks and advice and for kindly hosting me at Laboratoire de Physique des Solides, Université Paris-Sud. Special thanks to Prof. Michel Verdaguer and Dr. Valerie Marvaud for tons of samples and for educational discussions.

Thanks to Dr. Joan Adler for support in computational matters. I owe my friends Amit Kanigel and Adham Hashibon for their cooperation and much appreciated conversations. To my brothers Hanna, Tamer and Iyas, thank you.

I also wish to express gratitude to my parents Layla and Milad for their unconditional support through all my studies.

THE GENEROUS FINANCIAL HELP OF THE TECHNION, THE ISRAELI MINISTRY OF SCIENCE AND THE FRENCH ISRAELI COOPERATION PROGRAM AFIRST ARE GRATEFULLY ACKNOWLEDGED

Dedicated to Paula

Contents

List of Figures

List of Tables

Abstract

High spin molecules (HSM) are molecules consisting of ions coupled by ferromagnetic or antiferromagnetic interaction; these molecules crystallize in a lattice where neighboring molecules are very well separated, yielding at low temperatures (temperatures lower than the magnetic interaction between ions) molecules that behave like noninteracting giant spins. When these molecules have a magneto-crystalline anisotropy along the z axis, the energy of spin up and spin down states are equal. When the temperature is high enough the spin of the molecules can flip from spin up state to spin down sate thermally (over the anisotropy barrier), but when the temperature is much lower than the anisotropy barrier, the only possible relaxation mechanism is through tunneling. This behavior enables us to examine quantum effects on macroscopic properties, and is referred to as quantum tunneling of the magnetization (QTM).

Tunneling between different spin states can only be induced by terms in the spin Hamiltonian which do not commute with the spin in the z direction S_z. This term may be dipolar interaction between neiboring molecules, hyperfine interaction between nuclear spins and the electronic spin of the molecules, high order spin terms, tranverse magnetic field on the molecular spins etc...

In this work we aim at pointing out the term dominating QTM in anisotropic molecules by studying the spin dynamics in a family of simple isotropic high spin

molecules. These molecules are $CrCu_6$ with spin $S = 9/2$, $CrNi_6$ with spin $S = 15/2$, and $CrMn_6$ with spin $S = 27/2$.

We use DC-Susceptibility measurements to measure the magnetic properties of these molecules, and we perform muon spin lattice relaxation measurements using μSR and proton spin lattice relaxation measurements using NMR. We find that the spin dynamics in these molecules is independent of the spin value, strongly indicating that the spin dynamics at low temperatures is dominated by hyperfine interactions.

List of Symbols

J	:Magnetic coupling between ions inside a high spin molecule
S	:Quantum number of the total spin at the ground state
S_z	:Spin component in the z direction
$\mathcal{H}$	:Spin Hamiltonian
D	:Anisotropy parameter of the uniaxial term
E	:Anisotropy parameter of the rhombic term
k_B	:Boltzmann constant
T	:Temperature
$\vec{H}$	:External magnetic field
H_z	:The z component of the external magnetic field
H_x	:The x component of the external magnetic field
m	:Quantum number of the spin in the z direction
g	:The spectroscopic splitting factor
μ_B	:Magneton Bohr
t	:Time
τ^{-1}	:Tunneling rate
$\hbar$	:Plank's constant
c	:Sound velocity

ρ	:Specific mass
ω	:Frequency
T_1	:Spin lattice relaxation time
T_2	:Spin-spin relaxation time
Δ_0	:Tunnel splitting
P	:Tunneling probability
M	:Magnetization
χ	:Magnetic susceptibility
H_L	:Longitudinal magnetic field
H_T	:Transverse magnetic field
$A(t)$	:Asymmetry as a function of time
α	:Geometrical factor
$P_z(t)$	:Probe's polarization in the z direction as a function of time
$P(t)$	:Probe's polarization as a function of time
γ	:Gyromagnetic ratio
$B_\perp(t)$	:Local transverse field at probe's site
Δ	:RMS of local magnetic field at muon site
τ	:Field-field correlation time or spin state lifetime
ν	:Measurement frequency in an NMR experiment
$\|S, m>$	:Spin eigenstate with quantum numbers S and m
$E_{\mathbf{S},m}$	:Energy eigenvalue of spin state $\|S, m>$
$\tau_{S,m}$	:Lifetime of the state $\|S, m>$
$\mathcal{Z}$	:Partition function
A	:Coupling constant between the molecular and probe spin
$\mathcal{H}_{sp}$	:Spin phonon interaction Hamiltonian
$\vec{I}$	:Spin of the probe

Chapter 1

Preface

High spin molecules (HSM) are molecules consisting of ions coupled by ferromagnetic or antiferromagnetic interaction; these molecules crystallize in a lattice where neighboring molecules are very well separated. At temperatures lower than the magnetic coupling J between ions inside the high spin molecule, the spins of the ions are locked to each other, and the high spin molecules behave like noninteracting spins. The energy difference between the ground spin state and the next excited spin state is of the order of J, therefore at low temperatures only the ground spin state S is populated. This state is $2S + 1$ times degenerate in first order approximation. However at even lower temperatures the degeneracy can be removed by additional magneto-crystalline anisotropic interactions such as the uniaxial term DS_z^2, or rhombic term $E(S_x^2 - S_y^2)$ etc. When the temperature is high enough transitions between different spin states of the molecules are thermally activated, but when the temperature is much lower than the energy difference between spin states, the transitions between them are only possible through a quantum mechanical process.

In the cases where these molecules have a magneto-crystalline anisotropy, the energy of spin up and spin down states are equal. When the temperature is high enough the spin of the molecules can flip from spin up state to spin down sate thermally (over the anisotropy barrier), but when the temperature is much lower than the anisotropy barrier, the only possible relaxation mechanism is through tunneling. This behavior enables us to examine quantum effects on macroscopic properties, and is referred to as quantum tunneling of the magnetization (QTM).

The possibility of quantum tunneling of a large magnetic moment has been studied in small magnetic clusters[7, 8, 9, 10], which are comprised of particles with various magnetic sizes and properties. In contrast with most ensembles of small magnetic clusters, a sample of high spin molecules consists of a large number of chemically identical entities that are characterized by a unique set of parameters. This feature allows precise characterization of the sample [7, 11] and rigorous comparison with theory.

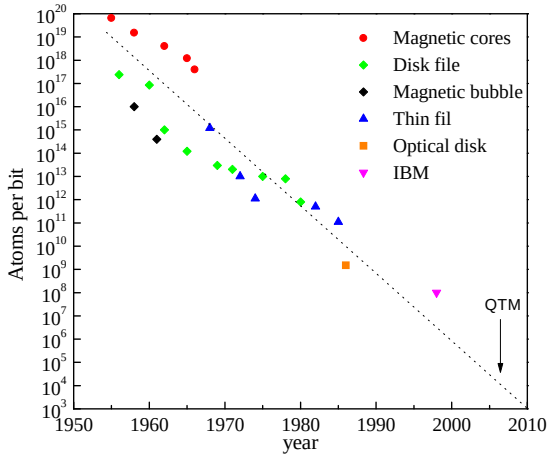

Figure 1.1: The atomic weight of a typical memory element, as a function of time [1, 2]

These nano-magnets could be applicable for the recording industry [2], as well as

in information transmission and computing [12]. Figure 1.1 shows the way in which magnetic computer memory elements have decreased exponentially in size over the last 40 years [2]. At present computers, as well as magnetic tapes, use elements which behave classically, and are stable over long periods of time. This stability exists over decades because they are big, and the energy barrier between two states of the element usually exceeds 100 k_BT even at room temperature. The hypothesized "quantum threshold", below which tunneling is significant even at $T = 0$, is supposed to consist of grains containing roughly $10^2 - 10^5$ spins, depending on the material involved.

In this chapter two of the most studied high spin molecules (Mn_{12} and Fe_8) will be introduced. These molecules show clear evidence for QTM (section 1.1). Then we will introduce the high spin molecules that we are studying (section 1.2), their chemical synthesis and magnetic properties.

1.1 Quantum Tunneling of the Magnetization in Mn_{12} and Fe_8

The Mn_{12} *acetate* compound, which is an example of HSM, whose formula $Mn_{12}O_{12}(CH_3COO)_{16}(H_2O)_4$, has been the subject of much interest since it was synthesized in 1980 [13]. This molecule contains four Mn^{4+} ($S = \frac{3}{2}$) ions in a central tetrahedron surrounded by eight Mn^{3+} ($S = 2$) ions, as shown in the inset of Figure 1.2. Oxygen bridges allow super-exchange coupling among the Mn ions, and magnetization measurements at low temperature indicate a total spin value of the Mn clusters of $S = 10$ [14, 15, 16], suggesting a simple picture of four inner ions

with their spins pointing in one direction and outer ions' spins pointing in the opposite direction. These molecules crystallize into a tetragonal lattice in which the distance between neighboring clusters is 7 Å, and the interaction between the clusters is negligible. Another compound in which QTM was observed is Fe_8, whose formula $[(tacn)_6Fe_8O_2(OH)_{12}]^{8+}$ [17]. Magnetic measurements show that Fe_8 has a ground spin state of $S = 10$ [4], which arises from competing antiferromagnetic interactions between the eight $S = \frac{5}{2}$ iron spins as shown in Figure 1.3.

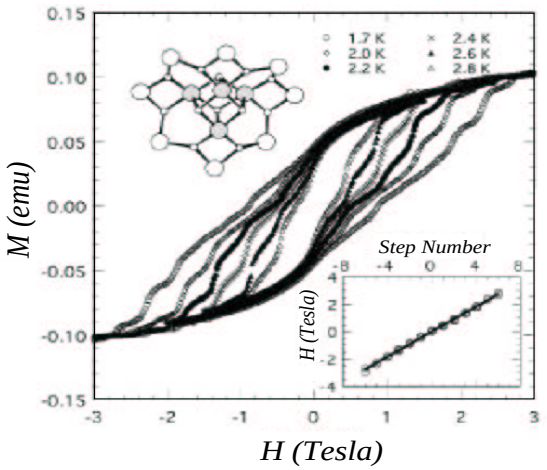

Figure 1.2: Magnetization of Mn_{12} as a function of magnetic field at six different temperatures, as shown (field sweep rate of 67 mT/min). The inset shows the field at which steps occur versus step number (with step 0 at zero field). The structure of the Mn_{12} molecule is represented at the top. Only the Mn^{4+} (large shaded circles), Mn^{3+} (large open circles), and oxygen (small circles) ions are shown (Taken from [3]).

Experiments on the two compounds Mn_{12} [3, 18, 19, 20] and Fe_8 [4, 21] show that the main part of the effective spin Hamiltonian of these compounds is [18, 19, 21],

$$\mathcal{H} = -DS_z^2 - g\mu_B H_z S_z \tag{1.1}$$

where D is the anisotropy constant, and the second term is the Zeeman energy. The values of D are found to be 0.547(3) K for Mn_{12} and 0.27 K for Fe_8. The eigenstates

of the Hamiltonian are the states $|m>$, where $S_z|m>= m|m>$ (seen in Figure 1.6). A simple calculation shows that the field for which two states, $|m>$ and $|m+n>$, are degenerate is

$$H_n = -\frac{nD}{g\mu_B} \tag{1.2}$$

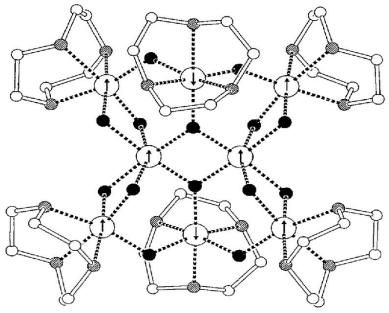

Figure 1.3: View of the structure of Fe_8: the large open circles represent iron atoms, while full, hatched and empty small ones stand for O, N, and C respectively. The spin structure of the $S = 10$ ground state is schematically represented by the arrows (Taken from [4]).

Figure 1.2 shows the magnetization of Mn_{12} as a function of the magnetic field for six different temperatures, with the magnetic field applied in the direction of the orientation of an oriented powder sample of Mn_{12}. Steps in the hysteresis loop can be seen as the field is increased; as the temperature is lowered new steps (with higher fields) appear, while steps with lower fields disappear. A linear fit (inset of Figure 1.2) indicates that there are steps at equal intervals of approximately 0.46 T [3].

For Fe_8 it was shown [4] that for temperatures lower than 400 mK the magnetization curve vs. the magnetic field exhibits a temperature independent hysteresis (for a fixed ramping rate $\frac{dH}{dt}$). Figure 1.4 shows two curves taken at 80 mK with two different ramping rates exhibiting hysteresis and steps at well defined field values,

similar to those seen in Mn_{12}. The steps for both ramping rates occur at the same field values, but the size of the step is different for different ramping rates.

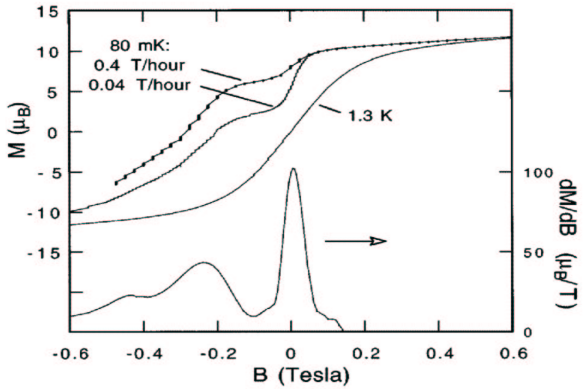

Figure 1.4: M vs. B: curve taken at 1.3 K shows no hysteresis. Below 400 mK curves are temperature independent, but depend on field ramp rate $\frac{dB}{dt}$ as shown. $\frac{dM}{dB}$ is shown for 0.04 T/h; peaks correspond to faster relaxation, verified by DC measurements (Taken from [4]).

When sweeping the magnetic field applied along the easy axis of a Mn_{12} of Fe_8 sample, from high negative to positive fields, and at very low temperatures, one obtains a considerable decrease in the relaxation time of the magnetization for certain magnetic fields, corresponding to those in which the steps are observed in the hysteresis loop [5] (e.g. for Mn_{12} see Figure 1.5). This decrease is due to the fact that at these fields equilibrium is reached faster. This behavior is attributed to quantum tunneling of the magnetization (QTM) within a simple model [22] of a double well with 10 spin up states corresponding to $m = +10, +9, \cdots, +1$ and 10 spin down states corresponding to $m = -10, -9, \cdots, -1$ (see Figure 1.6). The enhancement of the relaxation rate, as well as the steps in the hysteresis loop, can be understood within this simple model (more details will be given in chapter 2).

At high enough temperatures the reversal of the spin direction is thermally activated (over the barrier), so thermal fluctuations can bring the spin from one side of

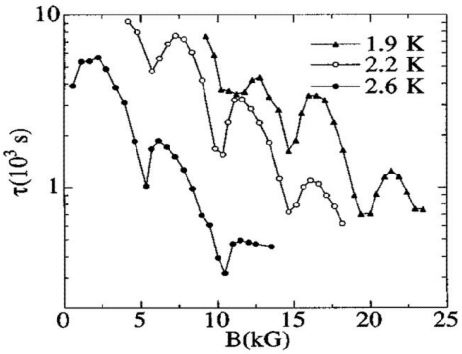

Figure 1.5: Field dependence of the relaxation time obtained from magnetic relaxation measurements at different temperatures in Mn_{12} (Taken from [5]).

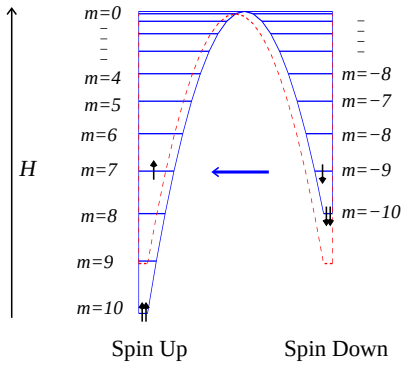

Figure 1.6: Potential well of Mn_{12} and Fe_8 crystals at $H = \frac{2D}{g\mu_B}$ (solid line) and at zero field (dashed line).

the double well to the other; while at low temperatures the reversal of the spin is due to tunneling between spin states, which can occur only between two spin states (on both sides of the double well) with the same energy level. If an external field is applied in the positive $\hat{z}$ direction, the states on the left side of the well ($m > 0$) are lowered, and on the right side ($m < 0$) are raised, as shown in Figure 1.6, and the relaxation of the magnetization is enhanced for fields that correspond to an amount of level shifting that brings two levels on both sides of the double well to match. However the spin Hamiltonian (1.1) commutes with S_z and hence cannot induce tunneling. Therefore one would expect tunneling between states to occur as a consequence of an additional part of interaction term, which is the issue dealt with in this work.

1.2 New Family of High Spin Molecules

In this work we study mainly a group of new HSM which allow for a variety of spin values and couplings between ions inside the molecule, but with similar chemical

structure.

1.2.1 Chemical Synthesis of the HSM

The chemical formula of the newly discovered family of nano-magnets we will study is $[B^{III}\{(CN)\text{-}A^{II}\text{-}L\}_n](An)_m$ where A^{II} could be V^{II}, Cr^{II}, Mn^{II}, Fe^{II}, Co^{II}, Ni^{II}, or Cu^{II}. And B^{III} could be Fe^{III}, Mn^{III}, or Cr^{III}, L is a ligand, and An is an anion which balances the molecules' charge [23]. In what follows we label the different compounds only as $B^{III}A^{II}_n$. This family is suited for our study since a large variety of spin values, atomic masses and nuclear spins could be produced. In addition one can introduce interactions between the magnetic clusters, as a test case. Three compounds have been successfully synthesized, $CrMn_6$ with total spin value $S = \frac{27}{2}$ [24, 25], $CrNi_6$ with total spin value $S = \frac{15}{2}$ [26, 25], and $CrCu_6$ with total spin value $S = \frac{9}{2}$[25].

1.2.2 Magnetic Properties of HSM

The cores of the compounds are presented in Figure 1.7. The chemical formulae of these compounds are $[Cr\{(CN)Cu(tren)\}_6](ClO_4)_{21}$, $[Cr\{(CN)Ni(tetren)\}_6\ ](ClO_4)_9$ and $[Cr\{(CN)Mn(tetren)\}_6](ClO_4)_9$, which we refer to as $CrCu_6$, $CrNi_6$ and $CrMn_6$ respectively. In these molecules a Cr(III) ion with $S = 3/2$ is coupled to six Cu ($S = 1/2$), Ni ($S = 1$) or Mn ($S = 5/2$) ions ferromagnetically (or anti-ferromagnetically in the case of $CrMn_6$) with a cyanide bridge, producing at low temperatures molecules with high spin ground state S. The coordination sphere of Cr and Cu/Ni/Mn can be described as a slightly distorted octahedral.

The high value S of these molecules is demonstrated in Figure 1.8, which shows the agreement between the field dependence of the magnetization of the three compounds

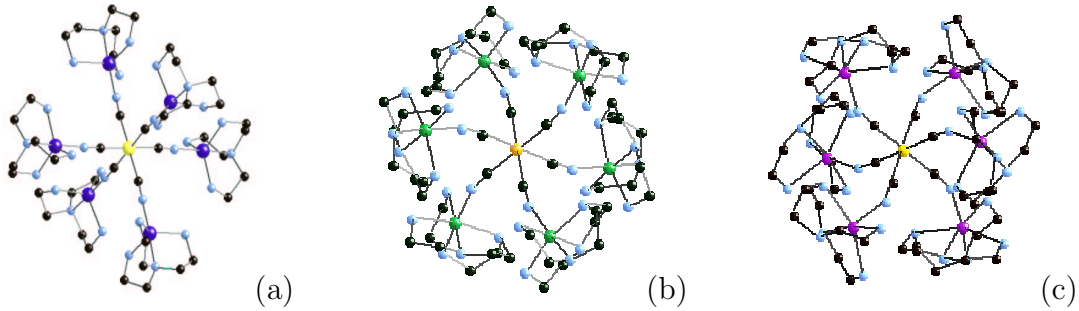

Figure 1.7: The (a) $CrCu_6$, (b) $CrNi_6$ and (c) $CrMn_6$ molecules cores.

$CrCu_6$, $CrNi_6$ and $CrMn_6$, with the corresponding Brillouin functions of spin 9/2, 15/2 and 27/2. The measurements were taken at $T = 2$ K, and demonstrate that at this temperature the molecule behaves like one giant magnetic moment.

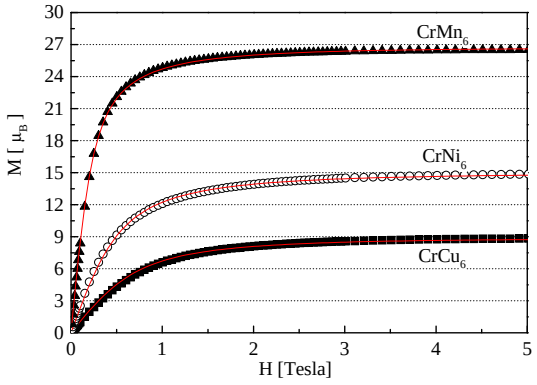

Figure 1.8: The magnetization vs. the magnetic field H, at temperature $T = 2$ K for the three compunds. The fits (solid lines) are the corresponding Brillouin function described in the text.

Figure 1.9 shows the normalized static susceptibility at field 100 G multiplied by the temperature as a function of temperature for the three compounds. The

susceptibility was fitted to the expected susceptibility from the Hamiltonian

$$\mathcal{H} = \sum_i J_{\mathrm{Cr}-i} S_{\mathrm{Cr}} S_i - D S_z^2 - g\mu_B H_z S_z \tag{1.3}$$

where the sum is taken over the 6 Cu, Ni and Mn ions, and $S_z = S_{\mathrm{Cr}} + \sum_i S_i$ is the z component of the total spin of the molecule, J is the coupling between spin inside the molecule, D represents the anisotropy, and H_z is the field in z direction. The fits give the values $J_{\mathrm{Cr}-\mathrm{Cu}} \approx 77$ K, $J_{\mathrm{Cr}-\mathrm{Ni}} \approx 24K$ K and $J_{\mathrm{Cr}-\mathrm{Mn}} \approx -11$ K [23, 26, 25]. The values of D were $D \approx 0$ for all three molecules. Details of the fits will be given in section 5.2.

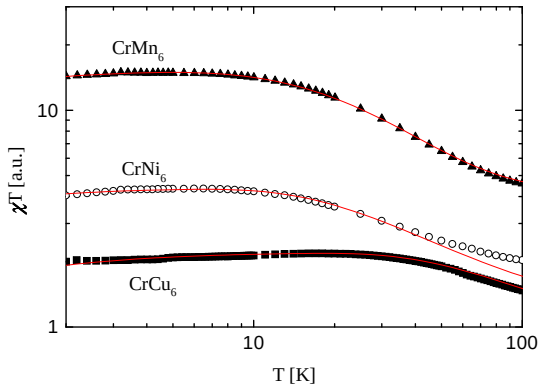

Figure 1.9: The normalized static susceptibility multiplied by the temperature for the compounds $CrCu_6$, $CrNi_6$ and $CrMn_6$.

Chapter 2

Theory of QTM

The Hamiltonian 1.1 commutes with the spin in the z direction, S_z, and therefore cannot induce tunneling. In this chapter I will present the different possibilities for additional terms to the Hamiltonian, which do not commute with S_z and induce spin tunneling in the anisotropic high spin molecules Mn_{12} and Fe_8.

2.1 Higher Order Spin Terms and Crystal Field Effect

One of the possibilities for the additional term which induces tunneling is the addition of a higher order spin term, depending on the symmetry of the lattice. In the case of Mn_{12}, the lowest order term allowed by the tetragonal symmetry of the lattice is [27, 28, 29, 30]

$$\mathcal{H}^t = BS_z^4 - C\left(S_+^4 + S_-^4\right) \tag{2.1}$$

where $B = -1.1 \times 10^{-3}$ K and $C = 2.9 \times 10^{-5}$ K. Similarly, for Fe_8, the D_2 symmetry suggests that the small correction spin term is [4, 31]

$$\mathcal{H}^t = E\left(S_x^2 - S_y^2\right) \tag{2.2}$$

where $E = 0.046$ K.

In 1986 a WKB formalism was presented by Van Hemmen *et al.* [32] to describe the quantum dynamics, including tunneling, of a single spin with large spin quantum number, and zero external magnetic field.

Consider the Hamiltonian

$$\mathcal{H} = -DS_z^l - \frac{g\mu_B}{2}\sum_{n=1}^{N} h_n\left(S_+^n + S_-^n\right) \tag{2.3}$$

with l an even integer, D and h_n positive constants. In the case of a strong anisotropy

$$D\sigma^l \gg g\mu_B \sum_{n=1}^{N} h_n \sigma^n \tag{2.4}$$

where $\sigma = \hbar S$ is the length of the classical spin, and for low energies $E \approx -D\sigma^l$, the WKB approximation gives a tunneling rate [33]

$$\tau^{-1} = \tau_0^{-1}\left(\frac{g\mu_B h_N \sigma^N}{2|E|}\right)^{\frac{2S}{N}} \tag{2.5}$$

where,

$$\tau_0^{-1} = \frac{lD\sigma^{l-1}}{2\pi} \tag{2.6}$$

Eq. (2.5) shows that the tunneling rate is universal, i.e. τ^{-1} depends on the anisotropy term $\mathcal{H}_0 = -DS_z^l$ only through the attempt frequency τ_0^{-1}, and is governed by the highest degree N of the transverse term [32].

For the Hamiltonian (2.3) with $l = 2$ at zero field, the tunneling rate between the two lowest spin states, within the WKB approximation, is

$$\tau^{-1} = \frac{DS\hbar}{\pi}\left(\frac{g\mu_B h_N (S\hbar)^{N-2}}{2D}\right)^{\frac{2S}{N}} \tag{2.7}$$

One should note that the spin Hamiltonian (1.1) with the term (2.1) (or (2.2)) cannot justify all the steps observed in the hysteresis loop in Mn_{12} (or Fe_8), as it couples only states differing by $\Delta m = \pm 4 \times n$ (or $\Delta m = \pm 2 \times n$), with an integer n. More importantly the tunneling rate due to the term (2.1) or (2.2) is proportional to S^S, which strongly depends on the value of the spin S.

2.2 Transverse Field Term

The appearance of the steps in Mn_{12} and Fe_8 hysteresis loops, for $\Delta m = \pm 1 \times n$, n being an integer number [34], indicates that the high order spin terms in the Hamiltonian (2.1) for Mn_{12} and (2.2) for Fe_8, do not fully explain the tunneling behavior in these clusters; therefore an additional term is needed to explain the observed possible transitions. Several authors have proposed a transverse field term [5, 31, 34]

$$\mathcal{H}^l = -g\mu_B H_x S_x = -\frac{g}{2}\mu_B (S_+ + S_-) \tag{2.8}$$

The tunneling rate as a results of (1.1) in addition to (2.8) has been calculated [35, 36] in longitudinal field $H_z = H_n$ (equation (1.2)) at $T = 0$. The tunneling splitting of each level m is given by [37]

$$\Delta E_m^n = \frac{2D}{[(2m-n-1)!]^2} \left(\frac{(S+m-n)!(S+m)!}{(S-m)!(S-m+n)!} \right)^{\frac{1}{2}} \left(\frac{g\mu_B H_x}{2D} \right)^{2m-n}. \tag{2.9}$$

The relation between ΔE_m^n and the tunneling rate τ is given by [33, 37]

$$\Delta E_m = \pi \hbar \tau^{-1} \tag{2.10}$$

and hence the tunneling rate at zero field, between the states $\pm m$, is

$$\tau^{-1} = \frac{\Delta E_m}{\pi \hbar} = \frac{2D}{\pi [(2m-1)!]^2 \hbar} \frac{(S+m)!}{(S-m)!} \left(\frac{g\mu_B H_x}{2D} \right)^{2m} \tag{2.11}$$

The Hamiltonian (1.1) in addition to (2.8) exhibits a crossover from the thermally activated regime to quantum tunneling regime [38, 39] that can be either first order (for $g\mu_B H_x < \frac{SD}{2}$) or second order (for $\frac{SD}{2} < g\mu_B H_x < 2SD$) [39]; which means sharp or smooth, depending on the strength of the transverse field H_x and the shape of the energy barrier (higher order corrections to DS^2).

Also here the spin dependence of tunneling rate due to the term (2.8) depends strongly on the spin value S.

2.3 Spin-Phonon Interaction

Tunneling induced by Spin-Phonon interaction was presented [27, 40] as an explanation for magnetic relaxation in Mn_{12}.

Consider an experiment in which the system is prepared in the spin state $|-S>$ (where $S_z|-S>=-S|-S>$) in an external negative magnetic field parallel to $\hat{z}$. At time $t = 0$ the field is reversed, and the system undergoes a transition to a different spin state $|m>$ (where $S_z|m>=m|m>$). According to [27] this transition is possible if a phonon of wave vector q is created, with an energy allowing for energy conservation

$$E_m + \hbar\omega_q = E_{-S} \tag{2.12}$$

where

$$E_m \approx -Dm^2 - 2\mu_B H_z m \tag{2.13}$$

If we consider small external magnetic fields satisfying $2\mu_B H_z < D$, for which equation (2.12) can be satisfied only for $m = S$, we obtain [27] the tunneling rate

$$\tau^{-1} = \frac{12}{\pi^2\hbar^4 c^5 \rho}|<S|V|-S>|^2 (H_z S)^3 \tag{2.14}$$

taking an isotropic dispersion law, $\omega_q = cq$; V is the spin-phonon interaction, and ρ is the specific mass.

Experimental results for the tunneling time τ as a function of the external field H_z in Mn_{12} show that τ increases with decreasing H_z for $H_z > 0.2$ T in qualitative agreement with (2.14), but at $H_z \simeq 0.2$ T, τ has a maximum and it decreases for smaller fields, as can be seen in Figure 1.5.

The argument above predicts a magnetization relaxation rate $\tau^{-1} \propto S^3$, ignoring hyperfine and dipolar fields; however even if these fields were taken into account it would not change the prediction of a minimum in τ^{-1} around $H_z = 0$, while experimentally it was observed in Mn_{12} and Fe_8 that the relaxation rate has a maximum at $H_z = 0$ [41]. Hence spin-phonon interaction cannot fully explain the tunneling behavior, though it may influence it.

2.4 Dynamic Nuclear Spin and Dipolar Interaction

Another attempt to explain the observed tunneling behavior is obtained by including dynamic hyperfine and dipolar fields. In the low temperature limit the ion spins in the high spin molecule are locked together, and the molecule behaves like one giant spin; however, due to dipolar fields the spin up and spin down states of the molecules are initially with different energies, and one needs the rapidly fluctuating hyperfine field to initially bring the spin up and spin down states to matching energies. The gradual adjustment of the dipolar fields across the sample, caused by tunneling relaxation, brings a steady supply of molecules further into resonance, allowing continuous relaxation.

This process is particularly important in Fe_8 where hyperfine couplings are weak compared to Mn_{12}. These arguments lead to a square root behavior of the magnetization at short times [41]

$$M(t) \propto \sqrt{\frac{t}{\tau}} \tag{2.15}$$

where τ depends on the nuclear T_2, the tunneling matrix element Δ_0 between the two lowest levels and the initial distribution of internal fields in the sample (which depends strongly on the shape of the sample), according to

$$\tau^{-1} \propto \frac{\Delta_0^2 T_2 |E_S - E_{-S}|}{E_D} \tag{2.16}$$

where E_D is total dipolar coupling from nearest neighbor molecules. The dipolar coupling is proportional to S^2 while $|E_S - E_{-S}| \propto S$, therefore the value of τ is expected to be proportional to S.

Recent experiments show a clear evidence for the effect of nuclear and dipolar fields on tunneling in Fe_8 [42], and a non-exponential relaxation of the magnetization was observed in both powder [4] and single crystal [42, 43] samples, as expected theoretically [41].

2.5 Landau-Zenner Tunneling

In the previous sections I presented the environmental influence of the molecular spin and its effect on the spin tunneling in these molecules. The Landau-Zenner model [44] can be applied to the experiments of swept external magnetic field, in which steps are observed in the hysteresis loop. In this model the off diagonal elements in the Hamiltonian, such as the interactions presented in the previous sections, introduce a gap (tunnel splitting) Δ_0 at the level crossing. The tunneling probability P in this

model is given by the Landau-Zenner formula [44, 45, 46]

$$P = 1 - \exp\left[-\frac{\pi\Delta_0}{4\hbar g\mu_B S(dH/dT)}\right] \tag{2.17}$$

where dH/dt is the field sweeping rate, $g \simeq 2$, μ_B the Bohr magneton.

This model reveals an extreme sensitivity of the tunnel probability to the Δ_0 and on the sweep rate, and can be used to measure the value of the tunnel splitting Δ_0 [47].

2.6 Summary

In this section I will summarize the results of the tunneling rates from the previous sections. In this work we are mostly interested in the dependence of the tunneling rate (or transition rate) between different spin states on the spin S of the HSM.

Interaction	*Spin dependence of the tunneling rate* τ^-1
High order spin terms	S^2 or higher
Spin-phonon	S^3
Static transverse field	higher than S^2
Dynamic hyperfine and dipolar	$1/S$

Table 2.1: The spin dependence of the tunneling rate for the different possible interactions presented in this chapter.

This work deals mainly with a group of isotropic HSM, which were presented in Section (1.2). Though no spin tunneling is observed in these molecules due to the absence of the anisotropic term DS_z^2, other interactions allowed by the symmetry of the molecules do exist, and can induce quantum transitions between different spin states of the molecule at very low temperatures.

This group includes three similar molecules with different spin values, therefore the spin dependence of the transition rates between the spin states, summarized in Table 2.1, will be an important indicator of the interaction dominating these transitions, and may shed some light on the dominant interaction which induces the tunneling in anisotropic HSM.

Chapter 3

Experimental Methods

3.1 DC Susceptibility Measurement

The magnetic measurements were performed using a Quantum Design's magnetic property measurement system (MPMS). This instrument uses a **S**uperconducting **QU**antum **I**nterface **D**evice (SQUID), which is the most sensitive device available for measuring magnetic fields. In this section I present the principles of operation of the MPMS following Ref. [48].

3.1.1 The SQUID

Due to the high sensitivity of the SQUID it should not be used to detect the magnetic field directly from the sample. Instead, the sample moves through a system of superconducting detection coils which are connected to the SQUID with superconducting wires, allowing the current from the detection coils to inductively couple to the SQUID sensor. When properly configured, the SQUID electronics produces an output voltage which is strictly proportional to the current flowing in the SQUID

input coil. Hence, the thin film SQUID device essentially functions as an extremely sensitive current-to-voltage converter.

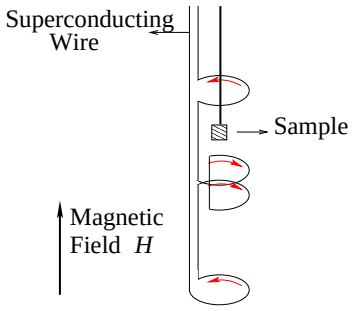

Figure 3.1: The second-order gradiometer superconducting detection coils

A measurement is performed in the MPMS by moving the sample through the superconducting detection coils (see Figure 3.1), which are located outside the sample chamber and at the center of the magnet (see Figure 3.2). As the sample moves through the coils, the magnetic moment of the sample induces an electric current in the detection coils. Because the detection coils, the connecting wires, and the SQUID input coil form a closed superconducting loop, any change of magnetic flux in the detection coils produces a change in the persistent current in the detection circuit, which is proportional to the change in magnetic flux. Since the SQUID functions as a highly linear current-to-voltage converter, the variations in the current in the detection coils produce corresponding variations in the SQUID output voltage which are proportional to the magnetic moment of the sample. In a fully calibrated system, measurements of the voltage variations from the SQUID detector as a sample is moved through the detection coils provide a highly accurate measurement of the sample's magnetic moment. The system can be accurately calibrated using a small piece of material having a known mass and magnetic susceptibility.

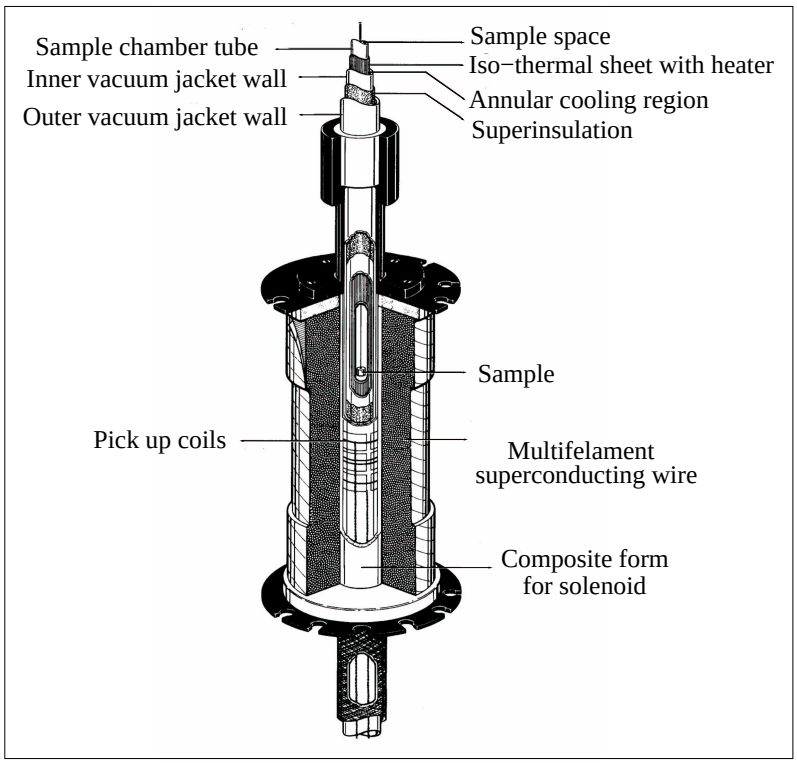

Figure 3.2: The configuration of the MPMS and location of the detection coil. The coil sits outside of the sample space within the liquid helium bath (taken from [48]).

3.1.2 The Superconducting Shield

Because of the SQUID's extreme sensitivity to fluctuations in the magnetic fields, the sensor itself must be shielded both from fluctuations in the ambient magnetic field of the laboratory and from the large magnetic fields produced by the superconducting magnet. The required magnetic shielding is provided by the superconducting shield which provides a volume of low magnetic field in which the SQUID and its coupling transformers are located. Proper operation of the SQUID does not necessarily require that the magnetic field inside the shield be extremely small, but it does require that any field inside the shield be extremely stable. Consequently, the superconducting shield serves two purposes in the MPMS:

1. To shield the SQUID detector from the magnetic field generated by the superconducting magnet.

2. To trap and stabilize the ambient laboratory magnetic field present when the SQUID and the superconducting shield are first cooled to liquid helium temperature.

The requirement for the superconducting shield can be more readily appreciated when one considers the sensitivity of the SQUID detector. The magnetic flux produced in the SQUID by a typical small sample is of the order of 0.001 of a flux quantum, where the flux quantum is 2.07×10^{-7} G-cm^2. For comparison, the magnetic flux through a 1 cm^2 area in the earth's magnetic field corresponds to about 2 million flux quanta.

3.1.3 The Superconducting Detection Coil

The detection coil is a single piece of superconducting wire wound in a set of three coils configured as a second-order (second-derivative) gradiometer. In this configuration, shown in Figure 3.1, the upper coil is a single turn wound clockwise, the center coil comprises two turns wound counter-clockwise, and the bottom coil is a single turn wound clockwise. When installed in the MPMS, the coils are positioned at the center of the superconducting magnet outside the sample chamber such that the magnetic field from the sample couples inductively to the coils as the sample is moved through them. The gradiometer configuration is used to reduce noise in the detection circuit caused by fluctuations in the large magnetic field of the superconducting magnet.

The gradiometer coil set also minimizes background drifts in the SQUID detection system caused by relaxation in the magnetic field of the superconducting magnet. If

the magnetic field is relaxing uniformly, then ideally the flux change in the two-turn center coil will be exactly canceled by the flux change in the single-turn top and bottom coils. On the other hand, the magnetic moment of a sample can still be measured by moving the sample through the detection coils because the counter-wound coil set measures the local changes in magnetic flux density produced by the dipole field of the sample. In this application a second-order gradiometer (with three coils) will provide more noise immunity than a first-order gradiometer (with two coils), but less than a third-order gradiometer (which would employ four coils).

It is important to note that small differences in the area of the counter-wound coils will produce an imbalance between the different coils, causing the detection coil system to be somewhat sensitive to the magnetic field from the superconducting magnet. In practice, it is never possible to get the coils exactly balanced against the large fields produced by the magnet, so changes in the magnetic field will always produce some current in the detection coil circuit. Over long periods of time and many measurements, large persistent currents could build up in the detection coil, producing noise in the system when these large currents flow in the SQUID input coil. The MPMS system prevents this from occurring by heating a small section of the detection coil circuit whenever the magnetic field is being changed.

3.1.4 The Measurement Procedure

The sample is mounted in a sample holder that is attached to the end of a rigid sample rod. The top of the sample transport rod is attached to a stepper-motor-controlled platform which is used to drive the sample through the detection coil in a series of discrete steps. It is possible to use discrete steps because the detection coil, SQUID input coil, and connecting wires form a complete superconducting loop. A change in

the sample's position causes a change in the flux within the detection coil, thereby changing the current in the superconducting circuit. Since the loop is entirely superconducting, the current does not decay as it would in a normal conductor. During a measurement the sample is stopped at a number of positions over the specified scan length, and at each stop, several readings of the SQUID voltage are collected and averaged. The complete scans can be repeated a number of times and the signals averaged to improve the signal to noise ratio.

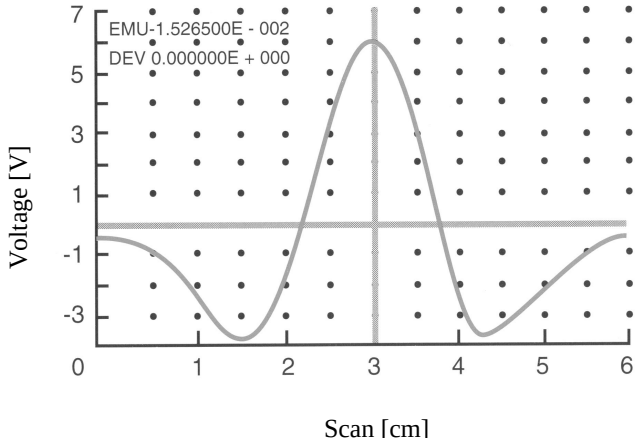

Figure 3.3: The output of the SQUID as a magnetic dipole is moved through the second-order gradiometer pickup coil. The vertical scale corresponds to the output voltage and the horizontal scale is sample's position (taken from [48]).

The currents induced in the detection coil are ideally those associated with the movement of a point-source magnetic dipole through a second-order gradiometer detection coil. The spatial (position) dependence of the ideal signal is shown in Figure 3.3 [48]. To observe this signal the sample should be much smaller than the detection coil and the sample must be uniformly magnetized.

The accurate determination of the magnetic moment of the sample from the SQUID output signal is made using computer fits. The linear regression method

makes a fit of the theoretical signal of a dipole moving through a second-order gradiometer to the actual SQUID output signal using a linear regression algorithm. This method requires the sample to remain well centered. When the sample is measured over a wide temperature range, the sample will change position due to changes in the length of its transport rod. Using software commands, the sample can be centered automatically.

3.1.5 Magnetic Units of Measure

The MPMS reports values of magnetic moment in e.m.u. which is equal to G×cm^3. We get the magnetization $\vec{M}$ by dividing the value of magnetic moment $\vec{m}$ by the volume V of the sample. The MPMS is calibrated with a sample of known magnetic moment in units of e.m.u., and all other signals are compared to the calibrated sample to get their magnetic moment in the same units. Another quantity frequently used in magnetism is the magnetic susceptibility, which is given by $\chi = M/H$, where H is the external magnetic field.

As an example we consider the Hamiltonian for paramagnetic moment in cgs units

$$\mathcal{H} = -\vec{m} \cdot \vec{B}. \tag{3.1}$$

Therefore the magnetic moment $\vec{m}$ is in units of erg/Gauss. The average spin value follows the relation

$$\vec{M}V = Ng\mu_B \left\langle \vec{S} \right\rangle \tag{3.2}$$

where N is the number of magnetic moments in the sample, from which $\left\langle \vec{S} \right\rangle$ is calculated by dividing the magnetic moment in e.m.u. units by $g\mu_B N$.

3.2 The Muon Spin Relaxation (μSR) Technique

The μSR technique allows one to study the magnetic properties of materials, through direct measurement of the time dependence of a positive muon (μ^+) polarization $P(t)$. The evolution of the polarization depends on the magnetic field experienced by the positive muon, and provides information on the magnetic environment in the vicinity of the muon. With this technique one can detect static magnetic field as small as a fraction of a Gauss and as large as several Tesla, and it is sensitive to magnetic fields fluctuating on a time scale of $10^{-3} - 10^{-11}$ sec.

3.2.1 Experimental Setup

The polarized muons are produced from pion decay (with pion lifetime $\tau_\pi = 26$ nsec) according to

$$\pi^+ \rightarrow \mu^+ + \nu_\mu$$

Since only left-handed neutrinos exist, and because pions have zero spin, muons produced by pions at rest ($p_\pi = 0$) have their spin $\vec{s}_\mu$ anti-parallel to their momentum $\vec{p}_\mu$ (See Figure 3.4). These muons are guided into the sample by a set of dipole mag-

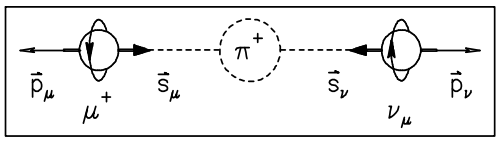

Figure 3.4: Schematic illustration for a positive pion decay into a muon and a neutrino (Taken from [6]).

nets; and come to rest in the sample within 10^{-10} sec, then each muon decays into a positron and two neutrinos:

$$\mu^+ \rightarrow e^+ + \nu_e + \bar{\nu}_\mu$$

mostly with a positron energetic enough to travel a substantial distance before annihilating, to reach the positron detectors.

The distribution of the decayed positrons is not spherically symmetric, but rather depends on the polarization of the muon, the positron is preferably emitted in the direction of the muon polarization as shown in Figure 3.5. In this figure the length

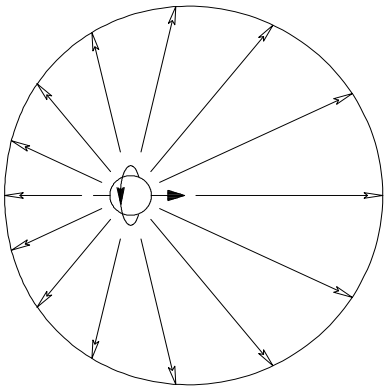

Figure 3.5: Angular distribution of positrons from muon decay (Taken from [6]).

of the arrow represents relative probability of positron emittance in the direction of the arrow. From the change in the angular distribution, as a function of time, of the emitted positrons, one can reconstruct the polarization of the muon as a function of time. When needed, we can also apply a variable external magnetic field, H_L along the initial polarization direction $\hat{z}$, or H_T transverse to $\hat{z}$.

3.2.2 The Longitudinal Field Configuration

The Longitudinal Field (LF) (also Zero Field (ZF)) experimental configuration (Figure 3.6(a)) is used to measure the rate in which the muon loses its polarization in the sample as a function of the magnetic field (H_L) applied along the direction of the initial muon polarization. This setup is based on the fact that at $t = 0$ positrons are

emitted into the forward (F) counter (full polarization) while at $t \longrightarrow \infty$ the polarization vanishes, and the positron counts in the forward (F) and backward (B) counters are equal. The positron counters are placed as shown in Figure 3.6(a). The forward counter has a small hole in it to allow the incoming muons to reach the sample.

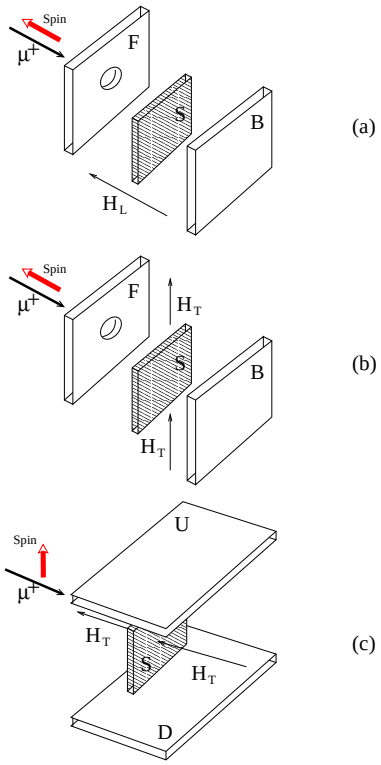

Figure 3.6: (a) Longitudinal (and Zero) field setup. (b) and (c) are Transverse field setups.

3.2.3 The Transverse Field Configuration

The transverse field (TF) experimental configuration (Figure 3.6(b) and (c)) is used to measure both the frequency of the muon precession and the rate in which it loses its polarization as a function of the magnetic field (H_T), applied perpendicular to the muons initial spin direction. There are two ways to achieve this configuration:

1. The counters are set up in a similar way to the LF configuration, but the field is applied in a direction perpendicular to the beam, as shown in Figure 3.6(b).

2. The muon spin is rotated by separators and the field is applied parallel to the beam. In this configuration the counters are placed above (U) and below (D) (or left and right sides) of the sample as shown in Figure 3.6(c).

3.2.4 Data Analysis

When the muons come to rest with their polarization along the beam direction $\hat{z}$, each muon spin evolves in the local field until the μ^+ decays at a time t after its arrival. The decay is asymmetric and the positron is emitted preferably along the muon spin direction. Two positron counters placed in the forward and backward directions with respect to $\hat{z}$ are used to obtain positron decay time histograms, which typically contain more than 10^6 events. The number of detected positrons in the backward and forward counters are, correspondingly,

$$\begin{aligned} N_B(t) &= N_0^B \left[B_B + e^{-\frac{t}{\tau_\mu}} (1 + A_0 P_z(t)) \right] \\ N_F(t) &= N_0^F \left[B_F + e^{-\frac{t}{\tau_\mu}} (1 - A_0 P_z(t)) \right] \end{aligned} \tag{3.3}$$

where B_B (B_F) is the time independent background in the backward (forward) counter, N_0^B (N_0^F) is the counting rate in the backward (forward) counter, $P_z(t)$ is the muon polarization in the z direction as a function of time and A_0 is the asymmetry.

To extract the polarization function we subtract the constant background ($N_0^B B_B$ and $N_0^F B_F$), to obtain

$$\begin{aligned} B(t) &= N_B(t) - N_0^B B_B \\ F(t) &= N_F(t) - N_0^F B_F \end{aligned} \tag{3.4}$$

We define the experimental "raw" asymmetry as:

$$\begin{aligned} A_r(t) &= \frac{B(t) - F(t)}{B(t) + F(t)} \\ &= \frac{(1-\alpha) + (1+\alpha)A_0 P_z(t)}{(1+\alpha) + (1-\alpha)A_0 P_z(t)} \end{aligned} \tag{3.5}$$

where α is the ratio of the raw count rates $\frac{N_0^F}{N_0^B}$, and reflects the ratio of effective solid angles of the detectors. α can be calculated by applying a magnetic field which is transverse to the initial muon polarization, and finding the α value that gives oscillations centered around zero.

Finally, from equation (3.5) one can extract the corrected asymmetry which is proportional to the polarization in the z direction

$$A(t) = A_0 P_z(t) = \frac{(\alpha-1) + (\alpha+1)A_r(t)}{(\alpha+1) + (\alpha-1)A_r(t)} = \frac{\alpha B(t) - F(t)}{\alpha B(t) + F(t)}. \tag{3.6}$$

The polarization in the perpendicular direction to $\hat{z}$ can be calculated from two positron counters placed up and down relative to the sample

$$A_\perp(t) = A_{\perp 0} P_\perp(t) = \frac{\alpha_\perp D(t) - U(t)}{\alpha_\perp D(t) + U(t)} \tag{3.7}$$

where $U(t)$ and $D(t)$ are the counts in the up and down counters after subtracting the background. $\alpha_\perp$ is the ratio between the raw count rate in the up detector to that in the down detector, $\frac{N_0^U}{N_0^D}$.

The asymmetry is fitted to the expected function from theoretical or phenomenological considerations, and the physical properties are extracted from the fitting parameters.

The arrangement of the positron counters and external field direction, longitudinal or transverse, is chosen depending on the information that we want to extract from the experiment.

3.2.5 Muon Spin Rotation

The fully polarized muon, after entering the sample, comes to rest in a magnetic environment. Since the mechanism which stops the muon is much stronger than any magnetic interaction, the muon maintains its polarization while loosing its kinetic energy. However, at the stopping site the muon spin starts to evolve in the local field $\vec{B}$. When all the muons experience a unique magnetic field in their site, the polarization along the $\hat{z}$ direction $G_z(t)$ is given by

$$G_z(t) = Re\left\{\cos^2\theta + \sin^2\theta e^{i\omega(t-t_0)}\right\} \tag{3.8}$$

where θ is the angle between the initial muon spin and the local field direction (see Figure 3.7), $\omega = \gamma_\mu B$ is the Larmor frequency of the muon ($\gamma_\mu = 85.162$ MHz/kG), and t_0 is the arrival time of the muon. When taking the powder average of Eq. (3.8) we get

$$G_z(t) = \frac{1}{3} + \frac{2}{3}\cos(\omega t) \tag{3.9}$$

where we took $t_0 = 0$.

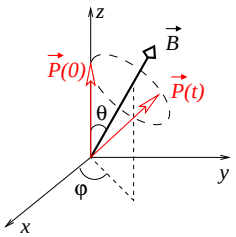

Figure 3.7: The $\hat{z}$ component of the muon polarization in the presence of a constant field $\vec{B}$.

In real systems, however, the local field experienced by different muons is rarely unique. It can vary from site to site as a result of nuclear moments, impurities, or non-homogeneous freezing of the ionic moments. It could also vary in time, at a given

site, due to dynamic fluctuations. In these cases the oscillation amplitude (2/3) and the average polarization (1/3) decay.

The decay or relaxation of the 2/3 component results from both dynamical fluctuations and spatial inhomogeneities. If we ignore momentarily the dynamical fluctuations, and assume that the frequency of oscillations, instead of being unique, follows the distribution $\rho(\omega - \omega_0)$, where ω_0 is the mean value of the Larmor frequency, then

$$G_z(t) = \frac{1}{3} + \frac{2}{3} \int d\omega \rho(\omega - \omega_0) \cos(\omega t). \tag{3.10}$$

It is easy to see that if ρ is Gaussian/Lorentzian the 2/3 component relaxes with a Gaussian/exponential line shape. Dynamical fluctuations could only add additional sources of relaxation. However, without the help of echo techniques (as in NMR) it is hard to distinguish between the two sources of relaxation of the 2/3 component.

On the other hand the spatial inhomogeneity of the field cannot cause relaxation of the 1/3 component since in the powder there are always 1/3 of the muons with their polarization pointing along the local field. These muons have a constant polarization unless the field changes with time. As a result, the relaxation of the 1/3 component could occur only from dynamical fluctuations of the local field.

3.2.6 Traditional Theory of Muon Spin Relaxation

The 100% polarization of the muons in the sample is not the equilibrium ratio of spin up to spin down and the muon gradually depolarizes in order to reach the equilibrium ratio. The time dependence of this depolarization is derived in this section using the strong collision model. In this model we assume that the field experienced by the muon changes discontinuously at times $t_1 < \cdots < t_n < t(= t_{n+1})$ with some average frequency ν. Between these field changes the polarization evolves as if the field

were static. We demonstrate the application of this model to two field distributions Gaussian and Lorentzian. The Gaussian distribution is given by

$$\rho^G(\vec{B}) = \left(\frac{\gamma_\mu}{\sqrt{2\pi\Delta^2}}\right)^3 \exp\left(-\frac{\gamma_\mu^2[\vec{B}-\vec{B}_0]^2}{2\Delta^2}\right) \tag{3.11}$$

where $\vec{B}_0$ is some average field which is either applied externally or caused by the magnetic moments in the sample, and Δ/γ_μ is the root mean square (RMS) of the field distribution. The Lorentzian distribution is given by

$$\rho^L(\vec{B}) = \left(\frac{\gamma_\mu}{\pi}\right)^3 \prod_{i=x,y,z}\left[\frac{a}{a^2+\gamma_\mu^2(B_i-B_i^0)^2}\right] \tag{3.12}$$

where B_i^0 is the i-th component of some average field $\vec{B}_0$, and a/γ_μ represents the width of the field distribution.

The static relaxation function $g_0(t)$ is obtained by convoluting $G_z(t)$ from Eq. (3.8) with the field distribution $\rho(\vec{B})$. For example, if $\vec{B}_0 = 0$ we obtain in the case of Gaussian distribution

$$g_0^G(t) = \int d^3B\rho^G(\vec{B})G_z(t) = \frac{1}{3} + \frac{2}{3}(1-\Delta^2t^2)\exp\left(-\frac{\Delta^2t^2}{2}\right). \tag{3.13}$$

This relaxation is known as the static Gaussian Kubo-Toyabe [49]. This function has a 2/3 component showing a damped oscillation around B, with time scale $1/\Delta$, and a persisting 1/3 polarization which is referred to as recovery. The RMS Δ of magnetic fields can be estimated from the rate of the damped oscillation.

In the case of Lorentzian distribution we obtain

$$g_0^L(t) = \int d^3B\rho^L(\vec{B})G_z(t) = \frac{1}{3} + \frac{2}{3}(1-at)\exp(-at). \tag{3.14}$$

This relaxation is known as the static Lorentzian Kubo-Toyabe [50, 51]. This function has a shallow "dip" of the damped oscillation compared to the Gaussian Kubo-Toyabe

(3.13), corresponding to a faster damping due to a wider range of fields B, with a time scale $1/a$, and then a recovery of 1/3 of the polarization follows.

Application of a longitudinal field H_L parallel to $\hat{z}$ helps aligning the local field along the z axis. The LF relaxation function for a Gaussian local field becomes [52]

$$g_z^G(t, H_L) = 1 - \left(\frac{2\Delta^2}{\omega_L^2}\right)\left[1 - e^{-\Delta^2 t^2/2}\cos(\omega_L t)\right] + \left(\frac{2\Delta^4}{\omega_L^3}\right)\int_0^t e^{-\Delta^2 t^2/2}\sin(\omega_L \tau)d\tau \tag{3.15}$$

where $\omega_L = \gamma_\mu H_L$. When Δ/ω_L is small, i.e. when the external field H_L is much higher than the internal field, the polarization approaches 1. This effect is called decoupling.

The LF relaxation function for a Lorentzian local field follows [53, 54]

$$\begin{aligned} g_z^L(t, H_L) &= 1 - \frac{a}{\omega_L} j_1(\omega_L t)e^{-at} - \left(\frac{a}{\omega_L}\right)^2\left[j_0(\omega_L t)e^{-at} - 1\right] \\ &- \left[1 + \left(\frac{a}{\omega_L}\right)^2\right] a\int_0^t j_0(\omega_L \tau)e^{-a\tau}d\tau \end{aligned} \tag{3.16}$$

where j_0 and j_1 denote spherical Bessel functions. When a/ω_L is small, i.e. when H_L is much higher than a, the polarization approaches 1, similar to the LF relaxation function for a Gaussian local field.

If we now take the field changes into account, then the polarization at a measured time t contains contributions from muons that experience no field changes at all, those that experience one change, two changes and so on. The probability that the field stays unchanged during the time $t_{i+1} - t_i$ is given by $\kappa(t_{i+1} - t_i)$. For Markovian processes we have

$$\kappa(t) = e^{-\nu t}. \tag{3.17}$$

It should be pointed out that this type of dynamical process (Markovian) leads to an exponential decay of the time-dependent field-field correlation function $\left\langle \vec{B}(t) \cdot \vec{B}(0) \right\rangle$.

The average polarization is obtained by taking the sum over all possible number of changes, weighted by their probability. Since the probability density for n changes between $[t_1, t_1 + dt_1], \cdots, [t_n, t_n + dt_n]$ is

$$\prod_{i=1}^{n} \exp\left[-\nu(t_i - t_{i-1})\right] \nu dt_i = \nu^n e^{-\nu t} \prod_{i=1}^{n} dt_i$$

we get

$$P_z(t) = e^{-\nu t}\left[g_0(t) + \nu \int_0^t dt_1 g_1(t_1, t) + \nu^2 \int_0^t dt_2 \int_0^{t_2} dt_1 g_2(t_1, t_2, t) + \cdots\right] \tag{3.18}$$

where $g_n(t_1, \cdots, t_n, t)$ is the polarization function given that the muon experiences field changes at $t_1, \cdots, t_n$. If we now assume that the fields at different time intervals are uncorrelated, and that during each time interval the polarization propagates according to the static function $g_0(t)$ we have

$$g_n(t_1, \cdots, t_n, t) = \prod_{i=1}^{n+1} g_0(t_i - t_{i-1}). \tag{3.19}$$

Eq. (3.18) can be further simplified. However, in most cases we end up using numerical techniques at some point in order to obtain $P_z(t)$. Therefore we will not further simplify this equation here.

We refer to the polarization function which is obtained by applying the strong collision model to the static Kubo-Toyabe as the dynamical Kubo-Toyabe (DKT). The advantage of the DKT is that it is very practical for data analysis since it is not limited to a specific range of parameters. In real systems, where the dominant source of relaxation often varies with temperature between the dynamic and the static, the ability to account for the muon spin relaxation with a theory which treats both sources on the same footing, is very useful.

3.3 The Nuclear Magnetic Resonance (NMR) Technique

NMR and μSR are very similar techniques in their principle of operation. μSR has the advantage of being universal (independent of the studied sample). Its disadvantage is that the local probes (muons) are located in an unknown position. NMR has the advantage that the local probes (nuclei) are well located in the structure of the compound. However not all samples contain the same nuclei.

3.3.1 Experimental Setup

In an NMR experiment the sample is placed inside a coil (see Figure 3.8), and immersed in a static external magnetic field $\vec{H} = H_0\hat{z}$. This field polarizes the nuclear spins along the z axis. In addition to this field we apply a transverse magnetic field H_1 along the x axis, which is produced by running an alternating current in the coil L (see Figure 3.8), with frequency equal to the Larmor frequency, $\omega_L = \gamma_N H_0$, where γ_N is the gyromagnetic ratio of the studied nuclear spin. To do so we tune the resonance frequency of the circuit (Figure 3.8) by changing the capacitance of both capacitors C and C'. We keep the impedance of the power supply (50 Ω) matched to the impedance of the rest of the circuit, in order to get maximum power from the power supply into the circuit. To ensure these two conditions, one must have

$$C + C' = \frac{1}{\omega_L^2 L} \tag{3.20}$$

$$\frac{50}{R} = \left(1 + \frac{C}{C'}\right)^2 \tag{3.21}$$

where R is assumed to be small.

To understand the effect of H_1 on the nuclear spins, it is convenient to define a rotating frame of reference which rotates about the z axis at the Larmor frequency, ω_L. We distinguish this rotating coordinate system from the laboratory system by primes on the x and y axes, $x'y'$.

The advantage of looking at the problem from a rotating reference frame is its simplicity; e.g. a nuclear magnetization vector rotating at the Larmor frequency in the laboratory frame appears stationary in a frame of reference rotating about the z axis.

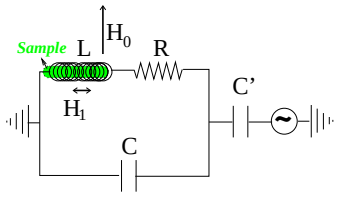

Figure 3.8: Resonance circuit for the NMR probe.

When the alternating current through the coil is turned on and off, it creates a pulsed H_1 magnetic field along the x' axis, this field can be seen as the sum of two components, one rotating clockwise and the other counterclockwise. It can be shown that only the component which is stationary in the rotating reference frame is important, and is taken into account. The spins respond to this pulse in such a way in order to cause the net nuclear magnetization vector to rotate about the direction of the applied H_1 field. The rotation angle depends on the length of time the field is on, τ, and its magnitude H_1

$$\theta = \gamma_N \tau H_1 \tag{3.22}$$

where τ is assumed to be much smaller than T_1 and T_2 (see below).

A $\frac{\pi}{2}$ pulse is one which rotates the nuclear magnetization vector clockwise by $\pi/2$

radians about the x' axis, down to the y' axis; while in the laboratory frame, the equilibrium nuclear magnetization spirals down around the z axis to the xy plane. One can see why the rotating frame of reference is helpful in describing the behavior of the nuclear magnetization in response to a pulsed magnetic field. Similarly a π pulse will rotate the nuclear magnetization vector by π radians. If the nuclear magnetization was initially along the z (x or y) axis it is rotated down along the $-z$ ($-x$ or $-y$) axis.

3.3.2 Pulse Sequences

The $\frac{\pi}{2}$ Free Induction Decay (FID) Pulse

In the $\frac{\pi}{2}$-FID pulse sequence, the net nuclear magnetization is rotated down into the $x'y'$ plane with a $\frac{\pi}{2}$ pulse. Then it begins to precess about the $+z$ axis, while its magnitude decays with time. This induces magnetic flux changes, and therefore induces a signal $\varepsilon(t)$ in the coil, which is then recorded. A timing diagram for a $\frac{\pi}{2}$-FID pulse sequence is a plot of signal versus time (in the rotating reference frame), as shown in Figure 3.9.

The signal $\varepsilon(t)$ follows

$$\varepsilon(t) = \varepsilon_0 e^{-\lambda t} \tag{3.23}$$

where λ represents the distribution of local magnetic fields experienced by the studied nuclei. The Fourier transform of the signal $\varepsilon(t)$ gives the NMR line in the frequency domain.

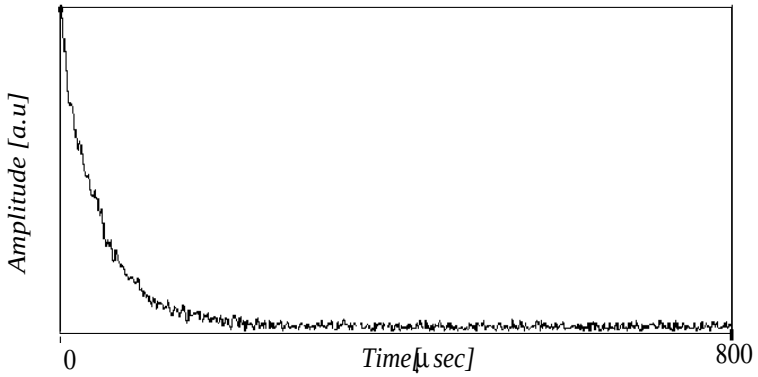

Figure 3.9: A $\frac{\pi}{2}$-FID signal from protons' nuclear spins in $CrNi_6$, at temperature $T = 300$ K and field $H_0 = 3.3239$ T.

The Spin-Echo Sequence and T_2 Measurement

Another commonly used pulse sequence is the spin-echo pulse sequence. Here a $\frac{\pi}{2}$ pulse is first applied to the spin system. The $\frac{\pi}{2}$ pulse rotates the nuclear magnetization down into the $x'y'$ plane. The transverse nuclear magnetization begins to dephase. At time t_{echo} after the $\frac{\pi}{2}$ pulse, a π pulse is applied. This pulse rotates the nuclear magnetization by π about the x' axis. The π pulse causes the nuclear magnetization to at least partially rephase and to produce a signal called an echo, as can be seen in Figure 3.10.

The dephasing of the transverse nuclear magnetization occurs because the spin packets making it up experience a time dependent magnetic field. The time scale of the dephasing is called the spin-spin relaxation time T_2.

To measure T_2 value we use the spin-echo sequence; by varying the time t_{echo}, and measuring the maximal value of the signal for the same parameters, $\varepsilon_{\max}(t_{\text{echo}})$. The maximal value of the signal as a function of t_{echo} behaves according to

$$\varepsilon_{\max}(t_{\text{echo}}) = \varepsilon_0 e^{-\frac{t_{\text{echo}}}{T_2}}. \tag{3.24}$$

In practice one measures $\varepsilon_{\max}(t_{\text{echo}})$. The values of $\varepsilon_{\max}$ as a function of t_{echo} are then fitted to a function of the form (3.24), or to a function of the form $f\left(\frac{t_{\text{echo}}}{T_2}\right)$, from which the value of T_2 is extracted.

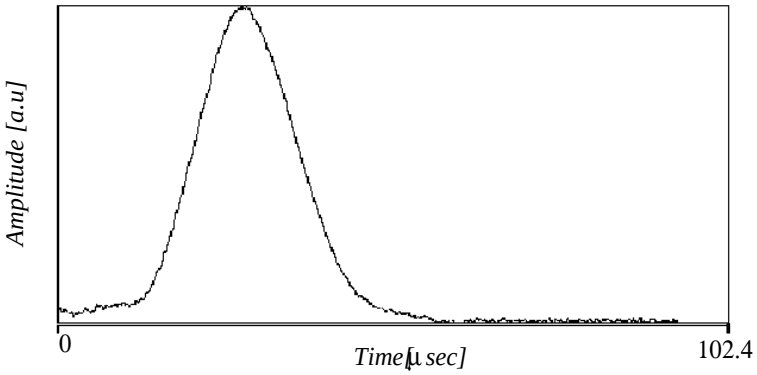

Figure 3.10: An echo signal from protons' nuclear spins in $CrNi_6$, at temperature $T = 160$ K and field $H_0 = 1.2$ T.

The Inversion Recovery Sequence and T_1 Measurement

In this sequence, a π pulse is first applied, this rotates the net nuclear magnetization down to the $-z$ axis. The nuclear magnetization undergoes spin-lattice relaxation and returns toward its equilibrium position along the $+z$ axis. Before it reaches equilibrium, a $\frac{\pi}{2}$ pulse is applied which rotates the longitudinal nuclear magnetization into the $x'y'$ plane. In this sequence, the $\frac{\pi}{2}$ pulse is applied at a time T_I after the π pulse. Once the nuclear magnetization is in the $x'y'$ plane it rotates about the z axis and relaxes giving a signal similar to that obtained in an FID.

The amplitude of the signal measured at a certain time t' as a function of T_I follows

$$\varepsilon(T_I) = \varepsilon_0 \left(1 - 2e^{-\frac{T_I}{T_1}}\right). \tag{3.25}$$

T_1 is called the spin lattice relaxation time, and it gives the time scale needed for the nuclear magnetization to reach thermal equilibrium. It should be noted that the zero crossing of this function occurs for $T_I = T_1 \ln 2$.

The signals obtained from measuring an inversion recovery sequence, as a function of the time T_I between the π and the $\frac{\pi}{2}$ pulses, and fixed parameters, behaves according to (3.25), fitting the signals as a function of T_I to the form (3.25), or to a function of the form $f\left(\frac{T_I}{T_1}\right)$, yields an estimate for T_1.

The Saturation Recovery Sequence and T_1 Measurement

This sequence gives another way to measure T_1, which is useful in the case of broad NMR lines and short T_1 values [55]. In this sequence multiple $\pi/2$ pulses (1-15 usually) are applied to obtain zero nuclear magnetization in the z direction, $M_z = 0$, and after a time T_I another $\pi/2$ pulse is applied.

After bringing the system to a state where $M_z = 0$, the system tries to go back to its thermal equilibrium state, where M_z is saturated, within a characteristic time T_1, and applying the last $\pi/2$ pulse at different values of waiting time T_I yields a signal amplitude which follows

$$\varepsilon(T_I) = \varepsilon_0 \left(1 - e^{-\frac{T_I}{T_1}}\right) \tag{3.26}$$

here the zero crossing of this function occurs for $T_I = 0$.

The signals obtained from measuring a saturation recovery sequence, as a function of the time T_I between the $\pi/2$ comb and the final $\pi/2$ pulse, with fixed parameters, behaves according to (3.26), and fitting the signals as a function of T_I to the form (3.26), or to a function of the form $f\left(\frac{T_I}{T_1}\right)$, yields an estimate for T_1.

3.3.3 Field Sweep and NMR Line Shapes

The NMR spectrum (or line shape) reflects the spectrum of frequency absorption of the studied nuclei, from which one can study the magnetic environment and interactions in the vicinity of the nuclei.

Fourier Transform

The NMR spectrum can be simply reconstructed by simply Fourier transforming the signal (echo or FID) in the rotating reference frame. This method is applicable in cases where the spectrum is narrower than the bandwidth of the receiving system.

Field Sweep

When the spectrum is broader than the bandwidth of the receiver one has to sweep the external magnetic field. By doing that one puts different groups of the nuclei in resonance, and scans the different sections of the NMR spectrum. The full spectrum is reconstructed by time integrating over different signals obtained for the different fields. Each integral corresponds to the intensity of the spectrum at the corresponding frequency.

Frequency Step and Sum (FSS) Method

This method is mostly useful for wide, in-homogeneously broadened NMR spectra [56]. It has the advantage of high resolution, high sensitivity and it extracts the distortions in the spectra introduced by the finite amplitude of the RF pulses and the finite bandwidth of the receiving system.

In this method we record the signal at a series of magnetic fields, changing the external magnetic field in equal steps. The final spectrum is reconstructed by Fourier

transforming each signal separately, shifting the frequency in correspondence to the field step, and then summing the spectra from all the field steps.

Chapter 4

Experimental Results

4.1 μSR Measurements in Fe_8

In this section we report clear evidence of QTM in single crystal Fe_8 using μSR technique. The high spin molecule Fe_8 has been studied extensively, since it exhibits "pure" tunneling, where temperature independent behavior is observed below 360 mK [4, 21, 43, 57].

At low temperature only the $S = 10$ spin state is populated. The energy levels of the Fe_8 spin states as a function of an external field H are shown in Figure 4.1. At certain "matching" field values $H_{\text{match}} = 0, \pm 2.1, \pm 4.2, \cdots$ T, states with different m values can have equal energies.

When applying a high positive field at low temperature, all molecules are polarized and occupy the $m = 10$ spin state. As the field is decreased nearly to zero, the spins remain in this state. However, when the applied field becomes negative the ground state changes to $m = -10$. As a result some of the spins tunnel from the $m = 10$ to the $m = -10$ state with probability $p(-10, 10)$. This tunneling takes place when the

field is close to the first matching field $H_{\text{match}} = 0$. Not all spins tunnel, and some stay in the $m = 10$ state with probability $1 - p(-10, 10)$. Transitions between different spin states are negligible when the external field is different from the matching fields [4]. Consequently spins have a chance to escape the $m = 10$ state only when the field is negative and equal to one of the matching fields H_{match}.

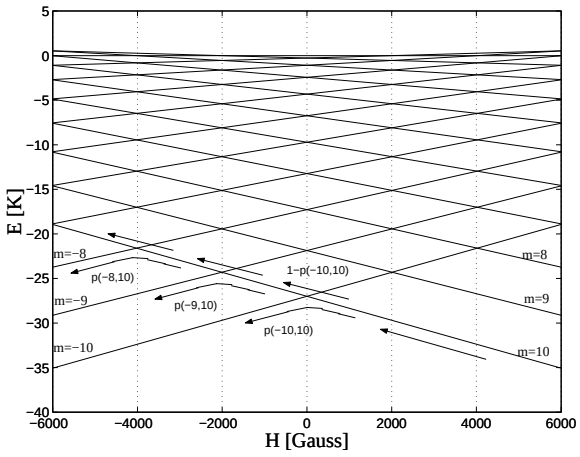

Figure 4.1: Energy levels of the different spin states of Fe_8 as a function of applied field $\vec{H} \parallel \hat{z}$

μSR measurements were performed on a few aligned Fe_8 single crystals which were glued on a small silver plate. The sample was then inserted into a brass cell with a mylar window (see Figure 4.3), and sealed inside with a He gas environment in order to ensure fast and uniform thermalisation of the sample and prevent it from shattering.

In these measurements we use the TF configuration (see section 3.2.3), in which we apply a magnetic field whose direction is 50^o relative to the initial polarization of the muon, but parallel to the easy axis $\hat{z}$ of the Fe_8 single crystals (see Figure 4.2). All measurements were performed at a temperature of 40 mK, to ensure that the Fe_8 molecules are in their $S = 10$ ground state and no thermal activation is possible.

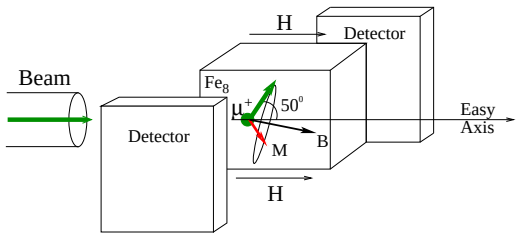

Figure 4.2: The arrangement of the Fe_8 single crystal in the experimental apparatus.

Each measurement was performed in three steps: (I) a field of $H = +2$ Tesla was applied for 15 minutes to polarize the Fe_8 molecules, (II) the field was swept to an intermediate negative magnetic field H_i with a sweep rate v, (III) eventually the field was swept back to $H = -50$ G, at which all measurements were performed. By performing step (II) the magnetic field passes through different matching field values, while step (III) guarantees that the changes in the local field experienced by the muons are a result of changes in the spin states of the surrounding Fe_8 molecules.

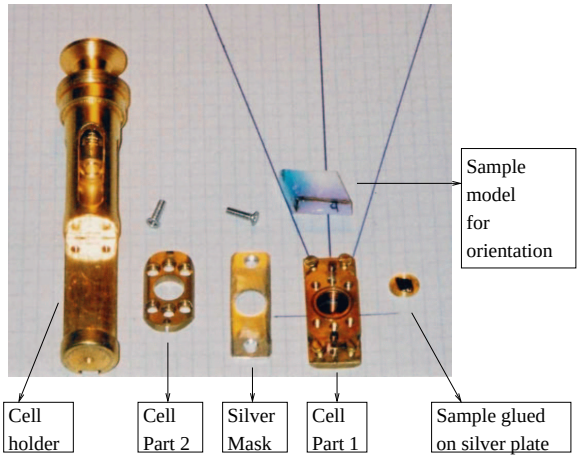

Figure 4.3: A brass cell with mylar window in which the Fe_8 sample was inserted

In Figure 4.4 we present the asymmetry as a function of time for different intermediate fields H_i. The field sweep rates is $v = 0.24$ T/min. In this figure one can

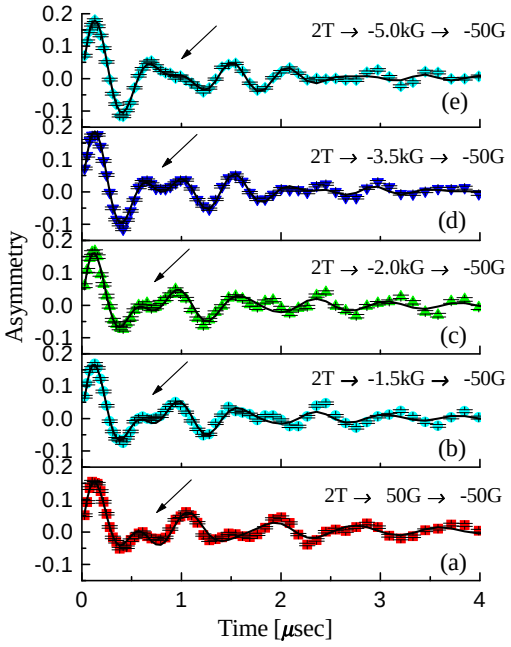

Figure 4.4: The asymmetry as a function of time for different values of $H_i = -0.05, -1.5, -2, -3, -5$ kG for (a), (b), (c), (d) and (e) respectively.

clearly see that depending on H_i the asymmetry is different (especially in the time range between 0.5 and 2 μsec), and that all asymmetries differ except for (b) and (c). The reason for that the number of matching fields crossed in both cases (b) and (c) is equal, and therefore there is no difference in the magnetization between these two cases. However, the runs (b) and (c) differ from the other runs, for which different matching fields were crossed.

We analyze the data by fitting the asymmetry of all runs to a function of the form

$$A(t) = A_0 \sin(\omega_0 t) e^{-\lambda_0 t} + A_1 \sin(\omega_1 t) e^{-\lambda_1 t} + B_g \tag{4.1}$$

where A_0, ω_0 and λ_0 represents the fraction of muons experiencing a magnetic field mainly from molecules with $m = 10$ spin state. Similarly A_1, ω_1 and λ_1 represent the fraction of muons which interact also with negative spin states. B_g is used to account for the baseline of the asymmetry. The precession frequencies ω_0 and ω_1 represent the different local fields experienced by the muons inside the Fe_8 single crystal. The changes in the frequencies indicate a change in the internal field, or in the spin direction of those Fe_8 molecules close to the muon and affecting its polarization.

The fitting curves are the solid lines in Figure 4.4, where the parameter $B_g \simeq 0$ was shared for all curves, the value of ω_0 was found to be 13.4(3) MHz, common to all curves, as expected for muons which do not experience a change in the local field. The values of A_0 and A_1 are presented in Figure 4.5. At low intermediate fields the

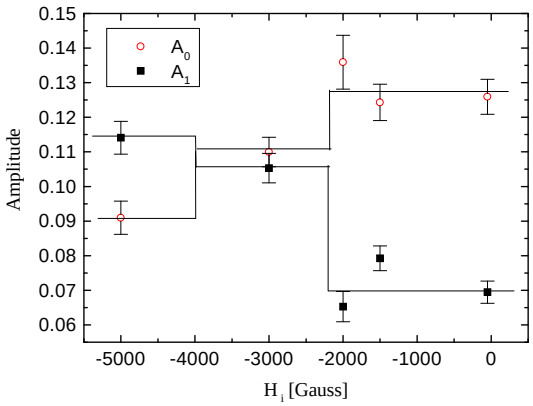

Figure 4.5: The amplitudes associated with the different fractions of muons. The amplitudes change only when different matching fields are crossed

amplitude A_0 is high while A_1 is low, indicating that most of the muons are interacting with Fe_8 molecules in the $m = 10$ spin state. A decrease in A_0 accompanied by an increase in A_1 is observed when more matching fields are crossed during the field cycle. More pronounced are the steps in the value of ω_1 presented in Figure 4.6,

where each step corresponds to a different matching field H_{match}.

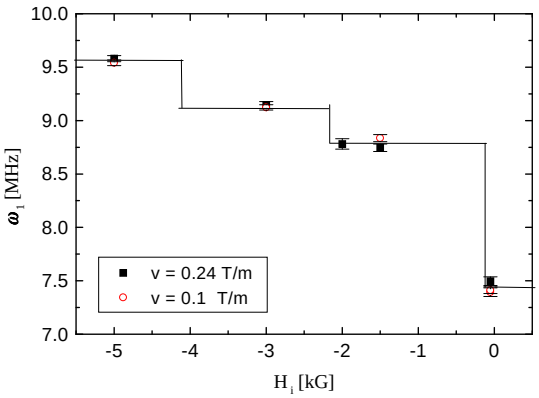

Figure 4.6: The value of ω_1 as a function of H_i for sweeping rate $v = 0.24$ T/min (squares) and $v = 0.1$ T/min (circles).

In order to rule out effects of superconducting magnet irreproducibility, we repeated the same measurements twice. We found that similar cycles reproduce the identical asymmetry, as seen in Figure 4.7(a), proving that the change in the frequency is not due to inaccuracy in the magnetic fields applied on the sample. Similarly, the effect of time dependence of the magnetization was ruled out by polarizing the spins of the Fe_8 molecules, after applying a field on +2 Tesla for 20 minutes, and then measurements at the same external field were taken, with intervals of 2 hours between them. As seen in Figure 4.7(b), no change in the asymmetry is observed even after 4 hours (while a single measurement takes 45 minutes), indicating that the time dependence of the magnetization is too small to account for the changes observed in the frequency in Figure 4.6.

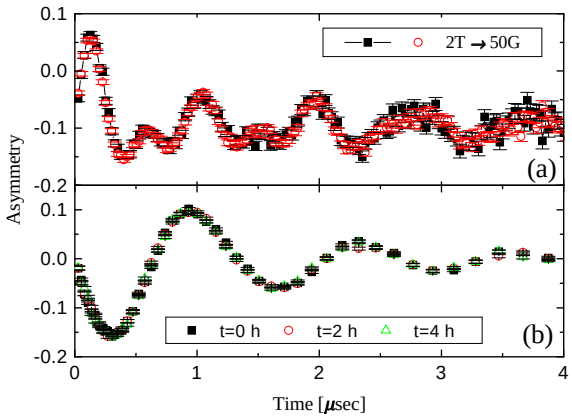

Figure 4.7: (a) Two similar measurements where we ramp the field up to +2 Tesla, then to −50 Gauss. Both measurements give the same asymmetry. (b) Measurements taken at different times after applying a field of +2 Tesla, and then ramping the field down to +50 Gauss. Even after 4 hours no change in the asymmetry is observed.

4.2 μSR Measurements in Isotropic Molecules

The μSR measurements reported here were performed in the LF configuration (see section 3.2.2), in which the magnetic field is applied in the direction of the initial muon polarization. In these experiments we measure the polarization (i.e. normalized asymmetry) $P(t, H)$ of a muon spin implanted in the sample, as a function of time t and magnetic field H (see section (3.2)), where $P(0, H) = 1$. The measurements in all molecules are performed at temperatures ranging from 25 mK up to 300 K, and in fields ranging between zero and 2 T. These experiments were performed at both ISIS and PSI, exploiting the long time window in the first facility for slow relaxation (high T), and the high time resolution in the second facility for fast relaxation (low T).

In Figure 4.8 we present the muon spin polarization as a function of time and for

different temperatures in $CrNi_6$ ($S = \frac{15}{2}$) at zero field (a), and at $H = 2$ T (b). In zero field, the relaxation rate increases, as the temperature is decreased, and saturates at ~ 5 K. In contrast, at $H = 2$ T, and temperatures lower than ~ 17 K, the relaxation rate decreases as the temperature is decreased, and does not saturate.

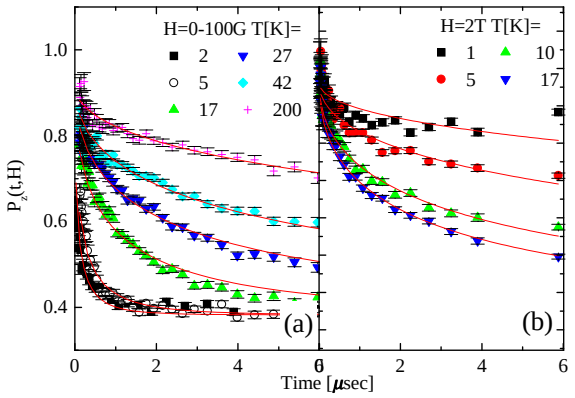

Figure 4.8: The spin polarization as a function of time. (a) At zero field and different temperatures. (b) At field $H = 2$ T and different temperatures. The solid lines are fits of the data to square root exponential functions.

The Hamiltonian of the isotropic HSM at zero field can be well approximated by

$$\mathcal{H} = -J \sum_{i=1}^{6} \vec{S}_0 \cdot \vec{S}_i, \tag{4.2}$$

at high temperatures the J bond between spins is broken, while at low temperatures, $k_B T \ll J$, the spins lie parallel or anti-parallel to each other, forming a ground spin state, with spin $\vec{S} = \sum_{i=0}^{6} \vec{S}_i$ and quantum spin number S, which is $2S + 1$ times degenerate.

The increase of the relaxation rate at high temperatures is caused by thermally activated transitions between excited spin states (e.g. $S = \frac{15}{2} \longrightarrow \frac{13}{2}$ etc.). However, at low temperatures, only the ground spin state is populated, and only transitions within the degenerate ground state are possible.

In Figure 4.9 we present the longitudinal field dependence of the muon polarization in $CrNi_6$ at $T = 50$ mK. The relaxation rate at this temperature decreases as the field is increased. Two aspects of the data indicate that the muon polarization relaxes due to dynamical field fluctuations; the first is that no recovery is observed, i.e. $\lim_{t\to\infty} P(t) \equiv P_\infty = 0$. A recovery of the polarization $P_\infty = P_0/3$ is expected in a case where the muon experiences a static local field and zero external field [58] (see section 3.2). The second is that the time scale of relaxation $1/\lambda$ in ZF is of the order 1 μsec; if this field were static it would have been of the order of $B \approx 10$ G (using $B = \lambda/\gamma_\mu$ where γ_μ is the muon gyromagnetic ratio, as seen in section 3.2.6). Such a field should have been completely decoupled ($\lim_{t\to\infty} P(t) = P_0$) with $\sim$ 100 G LF or more [58]. However, even fields as high as 5000 G do not decouple the relaxation. Therefore, we conclude that even at 50 mK the $CrNi_6$ spins are dynamically fluctuating. Similar experiments and line of arguments indicate that $CrCu_6$ and $CrMn_6$ spins are also dynamically fluctuating at very low temperature.

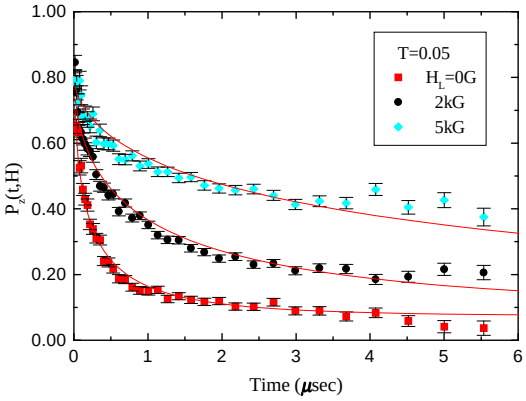

Figure 4.9: The variation of the polarization in $CrNi_6$ at $T = 50$ mK as the field is changed

We therefore analyze our data using spin lattice relaxation theory. In this theory,

one assumes a fluctuating local field $\vec{B}(t)$ experienced by a local probe (muon or nucleus) of spin $\vec{I}$. The spin lattice relaxation time T_1 in this case follows

$$\frac{1}{T_1} = \frac{\gamma^2}{2}\int_{-\infty}^{\infty} dt\,\langle B_\perp(0)B_\perp(t)\rangle \exp(i\gamma H t). \tag{4.3}$$

where γ is the gyromagnetic ratio of the local probe and H is the external field. The polarization of a local probe, in the fast fluctuation limit, is given by

$$P(H,t) = (P_0 - P_\infty)\exp\left[-t/T_1\right] + P_\infty \tag{4.4}$$

where P_0 is the initial polarization, P_∞ is the equilibrium polarization [54, 59],

$$T_1(H) = A + BH^2, \tag{4.5}$$

$$A = \frac{1}{\Delta^2\tau}, \tag{4.6}$$

$$B = \frac{\gamma^2\tau}{\Delta^2}. \tag{4.7}$$

The correlation time τ and mean square of the transverse field distribution at the probe site in frequency units Δ^2 are defined by

$$\gamma^2\langle B_\perp(t)B_\perp(0)\rangle = \Delta^2\exp\left(-t/\tau\right). \tag{4.8}$$

The fast fluctuation limit is obeyed when $\tau\Delta \ll 1$.

In μSR $P_\infty = 0$, and the muon could occupy many different sites in the sample, since the molecules are fairly large ($\sim$ 15 Å diameter) and present an organic surrounding around the metal ions and perchlorate anions separating the molecules. As a result one must average over Δ. Using the distribution [54]

$$\rho(\Delta) = \sqrt{\frac{1}{2\pi}}\frac{\Delta^*}{\Delta^2}\exp\left(-\frac{1}{8}\left[\frac{\Delta^*}{\Delta}\right]^2\right), \tag{4.9}$$

the resulting polarization is then

$$P(t) = \int_0^\infty P_0\exp\left(-t/T_1^\mu\right)\rho(\Delta)d\Delta \tag{4.10}$$

and allowing for a constant background (B_g) due to muons stopping outside the sample one obtains

$$P(t) = P_0 \exp\left(-\sqrt{t/T_1^\mu}\right) + B_g, \tag{4.11}$$

where $1/T_1^\mu$ is the muon spin relaxation rate. This form is in agreement with the experimental results (see below). In addition, Eq. (4.5) still holds, while in Eq. (4.6) and (4.7), Δ is replaced by Δ^*.

The solid lines in Figure 4.8 are fits of the data to Eq. (4.11) where P_0 is a global parameter. The parameter B_g is free within 10% of its mean value since the high fields affect the positron trajectory in a manner that is reflected in B_g. The fit is satisfactory in all cases except for the highest H and lowest T in $CrNi_6$. The relaxation rate $1/T_1^\mu$ in the different compounds, obtained from the fits is presented in Figure 4.10 as a function of temperature for different values of H. As pointed out above, $1/T_1^\mu$

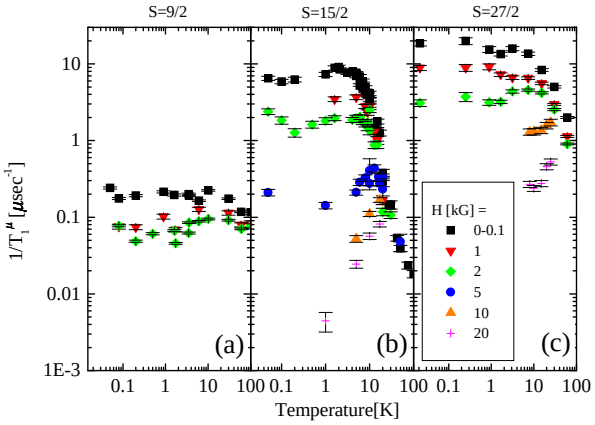

Figure 4.10: $1/T_1$ as a function of temperature for different external fields, measured by μSR in (a) $CrCu_6$ (b) $CrNi_6$ and (b) $CrMn_6$.

increases with decreasing temperatures, and saturates at low temperatures. The value of $1/T_1^\mu$ at the same field, for the different compounds, increases as the spin of the

compound is higher, as is expected due to the increase of the magnetic moment and hence the local field experienced by the muons. The saturation temperature increases as the coupling constant J increases. This is in strong contrast with Mn_{12} [60, 61] and Fe_8 [62] where in zero field $1/T_1^\mu$ increases continuously upon cooling until the correlation time τ becomes so long that the molecule appears static in the muon dynamical window.

In Figure 4.11 we plot the average relaxation time $T_1^\mu(H)$ at $T \to 0$ as a function of H^2 for all compounds, for fields up to 2 kG (note the axis break). We find that T_1^μ obeys Eqs. (4.5)-(4.7). This implies that the muon spin relaxation is indeed due to dynamical field fluctuations, and that at low T the field autocorrelation can be described by a single correlation time as long as the applied field is not too strong. At

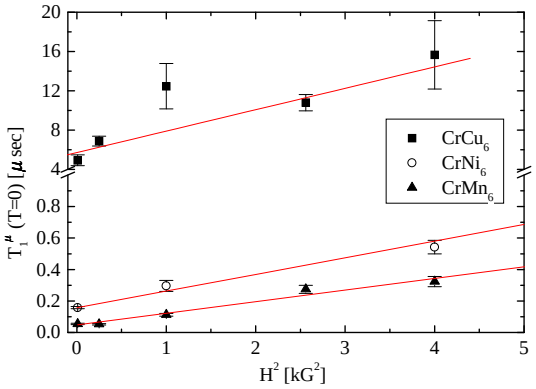

Figure 4.11: The saturation value of the spin lattice relaxation time as a function of H^2 for $CrCu_6$, $CrNi_6$ and $CrMn_6$. The solid lines are linear fits of the data.

high fields (> 2 kG) we find deviations (not shown) from the linear relation between T_1^μ and H^2. The deviation might be due to the impact of the field on the spin dynamics, *i.e.* the correlation function given by Eq. (4.8). From the linear fits in Figure 4.11, and taking $(\Delta^*)^2 = \gamma_\mu (AB)^{-1/2}$ from Eq. (4.6)-(4.7), where for a muon

$\gamma_\mu = 85.162$ MHz/kG, we find the values of Δ_0^* shown in Table 4.1. The subscript 0

Compound	Δ_0^* [MHz]	Δ_0^* [G]	τ_0 [nsec]
$CrCu_6$	4.9 ± 0.9	57 ± 10	7 ± 1
$CrNi_6$	26 ± 2	305 ± 25	10 ± 1
$CrMn_6$	38 ± 2	446 ± 24	11 ± 1

Table 4.1: The values of the average local field experienced by the muons Δ_0^* and the spin-spin correlation time τ_0 measured by μSR.

stands for $T \to 0$. Using $\tau = (B/A\gamma_\mu^2)^{1/2}$ from the same equations we find the values of τ_0 presented also in Table 4.1. These values of Δ_0^* and τ_0 are self consistent with the fast fluctuation limit. Most striking is the fact that all τ_0 values are very close.

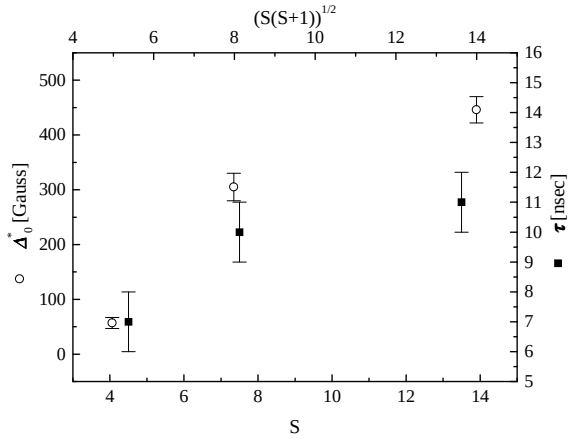

Figure 4.12: The values of Δ_0^* vs. $\sqrt{S(S+1)}$ (upper and left axes), and the values of τ_0 vs. S (lower and right axes).

The values of Δ_0^* and τ_0 are presented in Figure 4.12. One can see that the values of Δ_0^* increases with $\sqrt{S(S+1)}$, indicating that the muons, which experience the dipolar field of the molecular spin, stop in sites with a similar distance from the magnetic moments of the molecules in the three different compounds. The values of

τ_0 are very close but show a slight increase with the spin value S, indicating that the spin dependence of τ_0 is very weak.

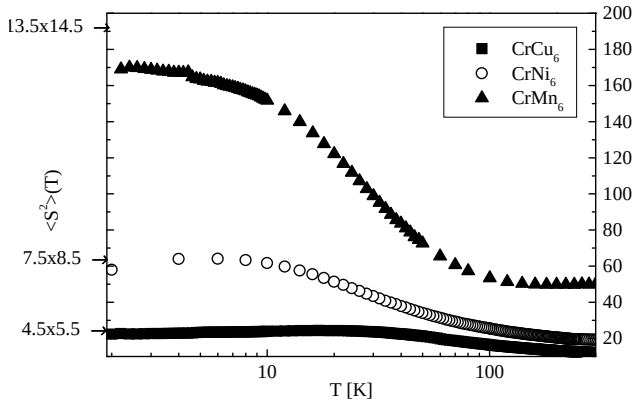

Figure 4.13: The value of $\langle S^2 \rangle (T)$ as obtained from Eq. (4.13) for the different compounds.

Finally, we would like to obtain the correlation time at all temperatures. This could be calculated from T_1^{μ} combined with magnetization measurements, at zero (or very low) fields. In zero order approximation we assume that $\langle B_{\perp}^2 \rangle$ is proportional to $\langle S^2 \rangle$ which is different from $S(S+1)$ since at temperatures $k_B T \sim J$, states other than the ground state S can be populated. Therefore in zero field

$$T_1^{-1}(T) = \frac{\Delta_0^{*2} \langle S^2 \rangle (T) \tau(T)}{S(S+1)}. \tag{4.12}$$

Taking

$$\left\langle S^2 \right\rangle (T) = \frac{3 k_B T \chi(T)}{N (g\mu_B)^2}, \tag{4.13}$$

where N is the number of molecules in the sample, μ_B is Bohr magneton, k_B is the Boltzmann factor, and $g = 2$, we find

$$\tau(T) = \frac{(g\mu_B)^2}{3k_B} \frac{S(S+1)}{T_1(T) T \chi(T) \Delta_0^{*2}}. \tag{4.14}$$

In Figure 4.13 we present $\langle S^2 \rangle (T)$ as a function of temperature for $CrCu_6$, $CrNi_6$ and $CrMn_6$, obtained from $H \to 0$ DC-susceptibility measurements and Eq. (4.13). In Figure 4.14 we present $\tau(T)$ as calculated using Eq. (4.14) for the different compounds. The T dependence of the correlation time $\tau(T)$, unlike the muon spin lattice relaxation rate, reflects the dynamics of the molecular spin without the T dependence of the field at the muon site. At $T \sim 100$ K there is more than an order of magnitude difference in τ between the different molecules. As the temperature is lowered the correlation time in all three compounds increases as the temperature is decreased, but reaches a *common saturation value* of ∼10 nsec (within experimental error) at $T \sim 10$ K. At this temperature only the ground state S is populated. In other words, when the HSM are formed at low T they have very close correlation times.

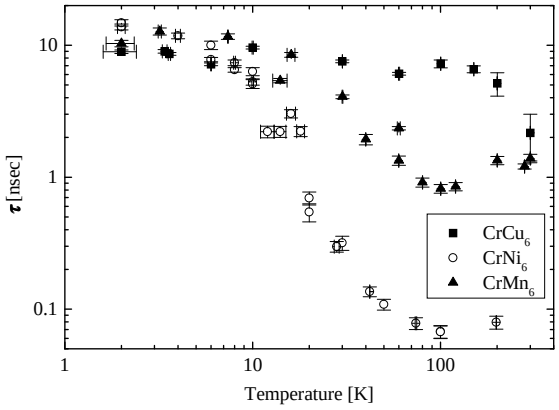

Figure 4.14: The correlation time τ as given by Eq. (4.14) as a function of temperature for $CrCu_6$, $CrNi_6$ and $CrMn_6$.

4.3 μSR Measurements in Gd

In this section we report on μSR experiments in $Gd(CF_3SO_3)_3$, a compound which is known to behave like a paramagnet. We refer to this compound as Gd. The paramagnetic behavior can be seen from measurements of the magnetization and susceptibility in Figure 4.15. From the saturation value of the magnetization curve at

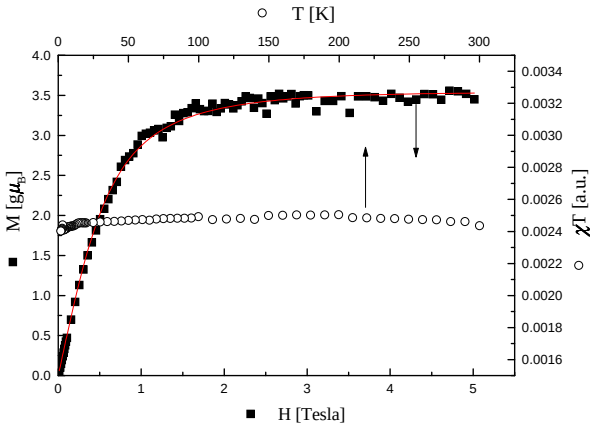

Figure 4.15: The magnetization vs. H and the susceptibility multiplied by the temperature as a function of the temperature in Gd. The solid line is the Brillouin function for spin $S = 7/2$.

$T = 2$ K as a function of the external field H one can see that the spin ground state of this compound is $S = 7/2$. The susceptibility multiplied by the temperature at field $H = 100$ Gauss shows no temperature dependence indicating the paramagnetic nature of the compound.

We studied this compound using the μSR technique as an example of a perfect paramagnet, and compare the muon spin lattice relaxation rate in a perfect paramagnet to that observed in the isotropic high spin molecules, especially at very low temperatures. The asymmetries obtained in these measurements were found to follow

an exponential behavior, and were fit to a function of the form

$$A(t) = A_0 e^{-\lambda t} + B_g \tag{4.15}$$

A_0 was taken as a common parameter for all curves, while B_g was allowed to vary slightly (less than 10%) to account for the effect of the external field on the value of α (see section 3.2) reflected in the value of B_g.

The spin lattice relaxation rate $\lambda = 1/T_1$ as a function of temperature for different external field values is presented in Figure 4.16. As expected the spin lattice relaxation rate is temperature independent and further no field dependence is observed.

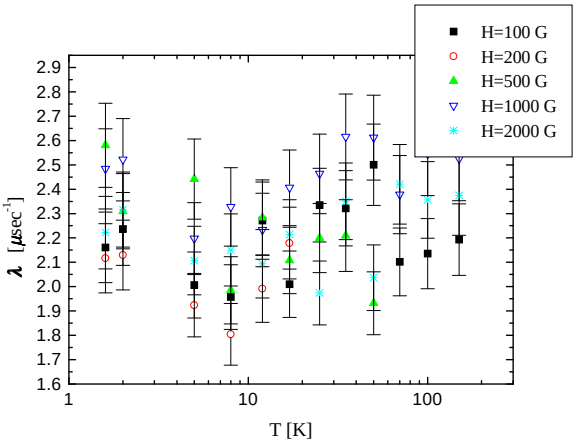

Figure 4.16: The spin lattice relaxation rate for muon spin in Gd.

The spin lattice relaxation rate in the isotropic high spin molecules shows similar temperature independent behavior at low temperatures. However, the effect of the external field in the case of the high spin molecules was more pronounced, this can be attributed to fast molecular spin fluctuations in the Gd compound, which are not affected by the external field.

4.4 NMR Measurements

In a μSR measurement it is hard to determine the stopping site of the muons, or the nature of its interaction with its surroundings, therefore the spin relaxation may be caused by muon diffusion or even muonium ($e^- - \mu^+$) formations, and not necessarily due to spin lattice relaxation. However, using NMR one can measure the spin lattice relaxation time of a local probe (nucleus) whose site is known, and compare it with μSR results. The disadvantage of NMR compared to μSR is that in the former one has to apply an external high field which couples to the spin of the molecules and influences the dynamics.

In this section I will present the results of proton-NMR measurements in all three compounds. The protons are most suitable in our case due to their chemical similarity to μ^+, with a different gyromagnetic ratio ($\gamma_H = 4.257$ MHz/kG) and different dipolar interaction with the magnetic surrounding.

4.4.1 $CrCu_6$

$CrCu_6$ has the lowest spin value among the isotropic HSM studied, therefore the dipolar interaction between the local probe $\vec{I}$ and the molecular spin $\vec{S}$, which decrease with decreasing spin $\vec{S}$, are smallest in this case. This gives us a possibility to better resolve the NMR lines in this case, the lines are less broadened and their features are sharper. This can be demonstrated by writing the dipolar interaction between the magnetic moment $\vec{m}$ of the molecule and the proton spin as a dipolar field $\vec{H}_{\rm dip}$ acting on the proton, where

$$\vec{H}_{\rm dip} = \frac{m}{r^3}\left(3\cos^2\theta - 1\right)\hat{z} \tag{4.16}$$

where r is the distance between the magnetic moment and the proton, and θ is the angle of the magnetic moment $\vec{m}$ relative to the proton spin (which is polarized in the direction of the external field). Since we are measuring a powder we expect a powder distribution probability of the angles θ of the magnetic moments

$$P(\theta)d\theta = \frac{\sin\theta}{2}d\theta$$

which is equal to the distribution probability of the local field experienced by the protons, $P(\theta)d\theta = P(H_{\rm dip})dH_{\rm dip}$. One can write

$$dH_{\rm dip} = \frac{dH_{\rm dip}}{d\theta}d\theta = \frac{6m}{r^3}\sin\theta\cos\theta d\theta$$

and therefore

$$P(H_{\rm dip}) = \frac{r^3}{12m\cos\theta} \tag{4.17}$$

but from Eq. (4.16) one obtains

$$\cos\theta = \sqrt{\frac{1}{3}\left(\frac{H_{\rm dip}r^3}{m}+1\right)}. \tag{4.18}$$

This gives the local field distribution (centered around the external field H)

$$P(H_{\rm dip}) = \frac{r^3}{12m}\left(\frac{H_{\rm dip}r^3}{3m}+\frac{1}{3}\right)^{-1/2} \tag{4.19}$$

However since $\theta \in [0,\pi]$, then $H_{\rm dip} \in [-2m/r^3, m/r^3]$. The observed NMR lines as a function of the field are a result of convoluting the receiver function (filtering etc.) with $P(H_{\rm dip})$, e.g. $P(H_{\rm dip})$ convoluted with a Gaussian of width $0.05m/r^3$, is presented in Figure 4.17.

The distance of the protons from the magnetic moment $\vec{m}$, governs the dipolar interaction and consequently the width of an NMR line. Thus one can differentiate between different groups of hydrogen in the studied compound, according to their distance from $\vec{m}$.

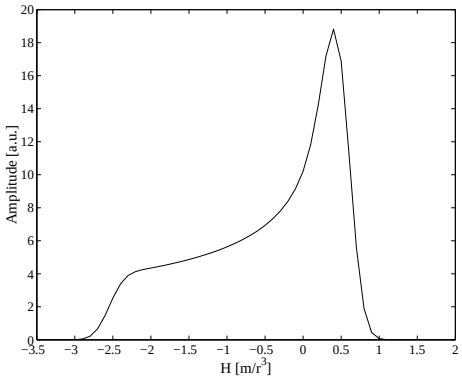

Figure 4.17: The NMR line-shape due to a dipolar interaction of the studied nuclei with a magnetic moment m.

In Figure 4.18 I present the NMR line at $T = 1.2K$ in $CrCu_6$, here one can identify three different hydrogen groups. Two of these groups show a dipolar line-shape (G1

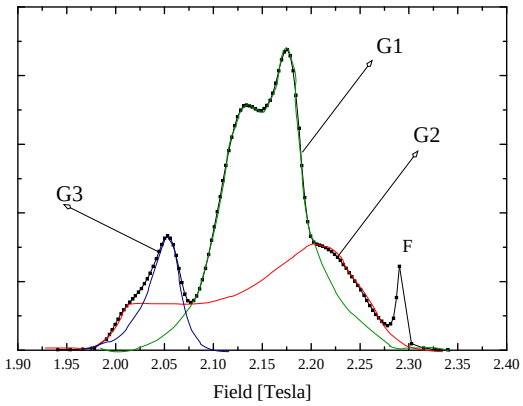

Figure 4.18: The proton NMR line at $T = 1.2$ K and field $H = 2.1542$ T ($\nu = 91.715$ MHz) in $CrCu_6$. The solid lines indicate the different groups G1, G2 and G3. F nuclei are from Teflon

and G2), as indicated in the figure, and the third exhibits a shift associated with hyperfine coupling of the protons to an electronic moment (G3).

In Figure 4.19 one can see the dependence of the line on temperature at field $H =$

2.1545 T (frequency $\nu = 91.715$ MHz). The lines broaden due to the increase of the molecular magnetic moment as expected from the static susceptibility measurements, but the shape of the lines is preserved, showing the three different hydrogen nuclei groups. One can see the saturation of the magnetization at low temperatures reflected in the saturation of the width of the lines.

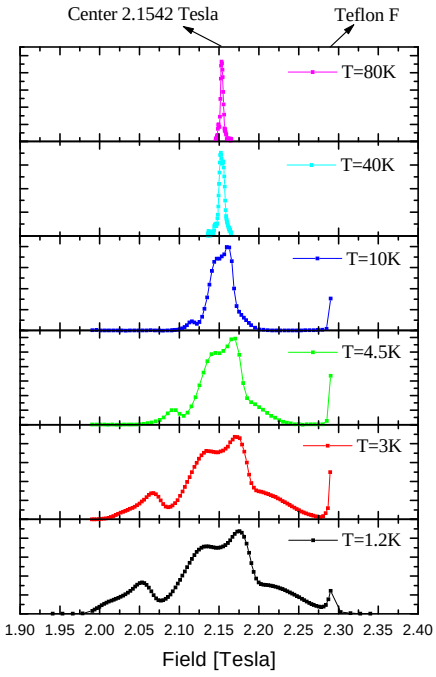

Figure 4.19: The proton NMR lines at different temperatures and field $H = 2.1542$ T ($\nu = 91.715$ MHz), in $CrCu_6$.

The group G1 is associated with a group of hydrogen bonded to carbon atoms (see Figure 4.20), which are on average $r(\text{G1}) = 3.8$ Å far from the Cu ions, the group G2 associated with hydrogen bonded to nitrogen atoms (see Figure 4.20), which is on average $r(\text{G2}) = 2.5$ Å far from the ions. The group G3 is associated with hydrogen nuclei of water, of which a small quantity is adsorbed into the compound, and is

located near magnetic moments.

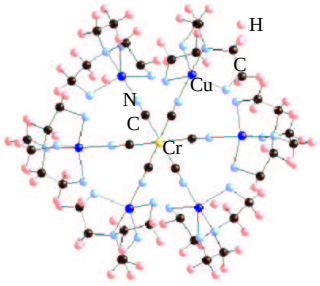

Figure 4.20: The $CrCu_6$ molecule. Yellow is Ni, dark blue is Cu, black is C, light blue is N and pink is H.

In Eq. (4.3) we present the spin lattice relaxation rate in relation to the time correlation function of the local field, if we assume that this field is that of the magnetic moment $\vec{m} = A < \vec{S} >$, and $\vec{B}(t) = A\vec{S}(t)/r^3$, then Eq. (4.3) can be written as [63]

$$\frac{1}{T_1} = \frac{\gamma_H^2 A^2}{2r^6} \int_{-\infty}^{\infty} \langle S_-(t) S_+(0) \rangle \, e^{i\omega t} dt \tag{4.20}$$

where $S_\pm$ are the raising and lowering spin operators and $\omega = \gamma_H H_0$. This indicates that the spin lattice relaxation rate is proportional to the dipolar interaction squared

$$\frac{1}{T_1} \propto \left(\frac{m}{r^3}\right)^2$$

and we expect that the ratio of T_1 values of two different protons groups is equal to the ratio of the average distance of the two different groups from the magnetic moment to the power 6, e.g. for the groups G1 and G2

$$\frac{T_1(\mathrm{G1})}{T_1(\mathrm{G2})} = \left(\frac{r(\mathrm{G1})}{r(\mathrm{G2})}\right)^6 \equiv n. \tag{4.21}$$

Saturation relaxation T_1 measurements in $CrCu_6$ were performed at $H = 2.1542$ T, and following the previous arguments we expect a double exponential relaxation,

where the ratio of the relaxation times is kept constant

$$S(t) = 1 - A_1 e^{-\frac{t}{T_1}} - A_2 e^{-\frac{t}{nT_1}} \tag{4.22}$$

where A_1 and A_2 are the amplitudes of the different groups' contributions to the signal and n is the ratio of the relaxation times of the two groups, defined by Eq. (4.21). Indeed the saturation relaxation was found to follow Eq. (4.22) with a common value of $n = 4.7$, for all temperatures and fields (e.g. see Figure 4.21). In Figure 4.22 the

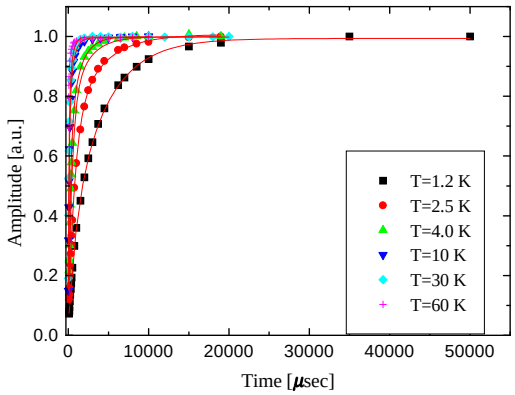

Figure 4.21: The saturation relaxation measurement results in $CrCu_6$ for different temperatures at $H = 2.1545$ T ($\nu = 91.715$ MHz). The solid lines are fits to a function following Eq. (4.22) with $n = 4.7$ (see text).

values of T_1 as a function of temperature and for different fields are presented. The value of ${}^6\sqrt{n} = 1.3$ was found to be in a very good agreement with the expected value from the average distances $3.49/2.55 = 1.36$.

Plotting the value of $\ln(1/T_1)$ versus the inverse temperature $1/T$ reveals that the low temperature part of this plot is linear for all measured fields, as seen in Figure 4.23. This indicates that the spin lattice relaxation at these temperatures and

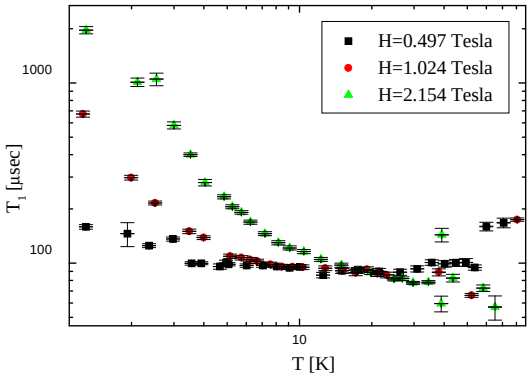

Figure 4.22: T_1 as a function of temperature for different external magnetic fields in $CrCu_6$.

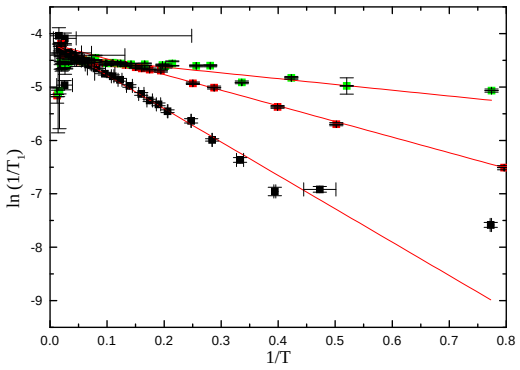

Figure 4.23: The value of $\ln(1/T_1)$ as a function of the inverse temperature for three different fields in $CrCu_6$.

fields is driven by thermal activation between the different spin states

$$\frac{1}{T_1} \propto e^{\frac{\Delta}{T}}. \tag{4.23}$$

Plotting the values of Δ obtained from the linear fits as a function of the external field H in Figure 4.24, indicates that Δ the activation energy is proportional to the field H, i.e. to the Zeeman splitting. The $CrCu_6$ molecule at these temperatures is found in its ground spin state $S = \frac{9}{2}$, and the spin lattice relaxation is due to transitions within this ground state and different S_z quantum numbers, as expected from the Hamiltonian 4.2, and J much higher than the temperature.

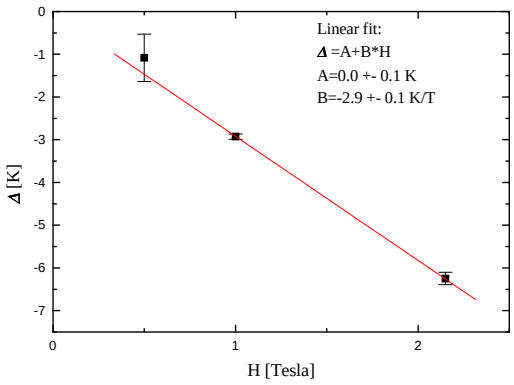

Figure 4.24: The value of the activation energy Δ of the spin lattice relaxation rate as a function of the external field

4.4.2 $CrNi_6$

Contrary to the case of $CrCu_6$, the proton NMR lines in $CrNi_6$ have less features. The lines presented in Figure 4.25 show an inhomogeneous broadening, as the temperature is decreased, but no distinct nuclei groups can be seen. The large number of nuclei groups and large magnetic moment of this molecule, yields NMR lines which are

comprised of a large number of broad lines. However, at temperatures lower than 20 K two different proton groups can be observed, a narrow line which we attribute to impurities in the studied sample, and the other is attributed to hydrogen nuclei around the Ni ions in the molecules.

The saturation relaxation curves measurement on the broad line part in this compound were found to follow a stretched exponential, which can be explained by the many in-distinguishable proton sites, while the relaxation of the narrow part was found to be much longer, indicating a very weak magnetic coupling of this group of nuclei with its surroundings, supporting its attribution to impurities.

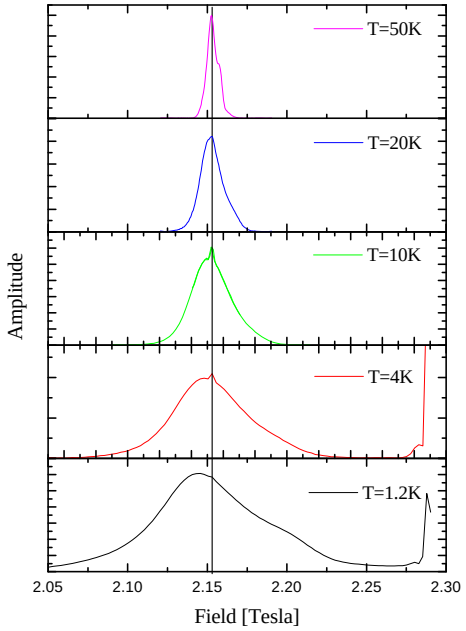

Figure 4.25: The proton NMR lines in $CrNi_6$, at different temperatures and external field $H = 2.1545$ T ($\nu = 91.715$ MHz).

We evaluated the spin lattice relaxation times T_1 of the protons belonging to the

broad part of the line, by fitting the relaxation curves to

$$S(t) = 1 - Ae^{-\left(\frac{t}{T_1}\right)^{\beta}} \tag{4.24}$$

where $\beta = 0.6 - 0.75$. The T_1 values as a function of temperature and for different

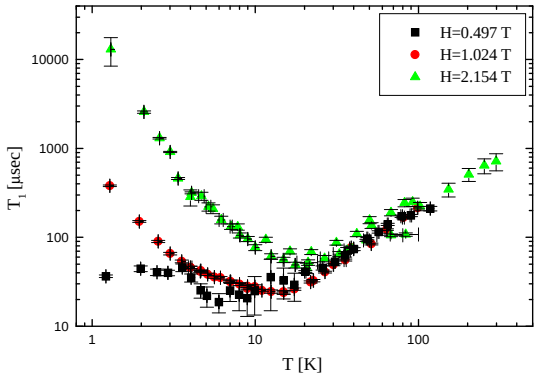

Figure 4.26: The values of T_1 as a function of temperature for different external fields in $CrNi_6$.

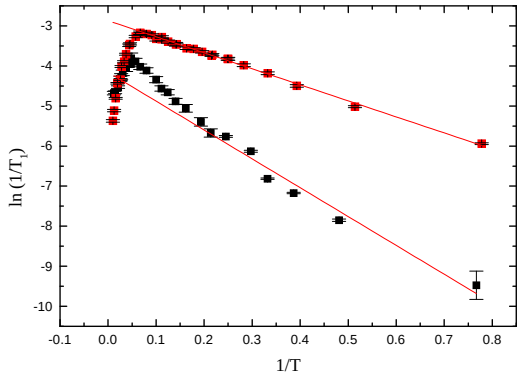

Figure 4.27: The value of $\ln(1/T_1)$ as a function of the inverse temperature for two different fields in $CrNi_6$

fields are presented in Figure 4.26. The values of T_1 with external field $H = 0.5$ T were found to be very short, and they should be taken qualitatively only.

Also in this case plotting $\ln(1/T_1)$ versus the inverse temperature $1/T$ reveals that for the fields $H = 1$ and 2 Tesla the low temperature part of this plot is linear, as seen in Figure 4.27. One can see that the spin lattice relaxation rate in this compound follows Eq. (4.23). The linear fits in Figure 4.27 show that the activation energy Δ is -7.2 K and -4 K at $H = 2$ and 1 T, respectively. Therefore also in this case Δ is proportional to the Zeeman splitting of the ground state.

4.4.3 $CrMn_6$

This compound has the highest spin ground state value, leading to a very short spin lattice relaxation times, which is considerably harder to measure by NMR, therefore the results presented here are of much lower quality compared to those presented for $CrCu_6$ and $CrNi_6$. However, the general temperature and field dependence of the spin lattice relaxation rate is similar to the results in the other two compounds.

The proton NMR lines show inhomogeneous broadening as the temperature is decreased, due to the high magnetic moment experienced by the protons. Similar to the case of $CrNi_6$ at temperature lower than 20 K two different proton groups can be distinguished as seen in Figure 4.28. The narrow line is attributed to impurities or water molecules adsorbed in the studied sample, while the broader line is attributed to protons in the molecule which experience the magnetic field from the local moments of the Mn ions.

The T_1 measurements in this compound were very difficult to carry out due to the extremely fast spin lattice relaxation. The relaxation curves were found to follow a

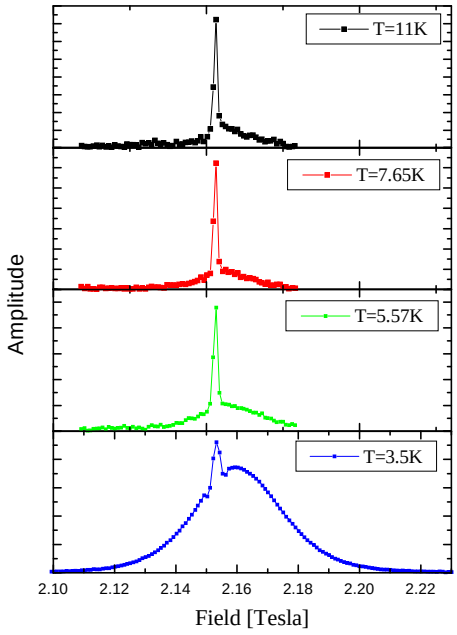

Figure 4.28: The proton NMR lines in $CrMn_6$, at different temperatures and external field $H = 2.1545$ T ($\nu = 91.715$ MHz).

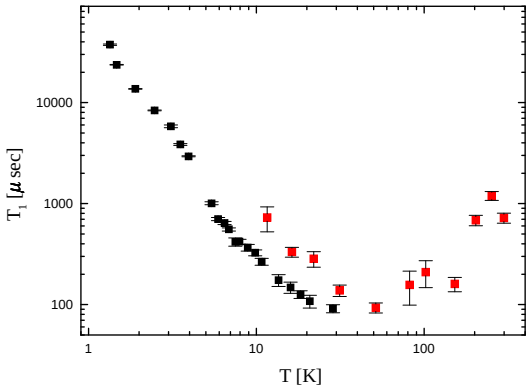

Figure 4.29: The values of T_1 as a function of temperature at $H = 2.1542$ T in $CrMn_6$.

stretched exponential behavior, similar to the case of $CrNi_6$. The spin lattice relaxation times were evaluated by fitting them to Eq. (4.24) with $\beta = 0.6 - 0.75$, and are presented in Figure 4.29.

4.5 Comparing μSR and NMR

Although our data support a picture where the muon spin relaxes due to dynamically fluctuating magnetic fields, they leave open the interpretation of these fluctuations. In order to address this question we compare the proton NMR $1/T_1^H$ measurements to $1/T_1^\mu$ measured using μSR.

Since the proton gyromagnetic ratio is very different from that of the muon, we scale the NMR results and plot them together with the μSR results in Figure 4.30, for $CrCu_6$ (a), $CrNi_6$ (b) and $CrMn_6$ (c). The scaling factor C used in Figure 4.30 is 0.02 for $CrCu_6$, 0.01 for $CrNi_6$ and 0.225 for $CrMn_6$. It was chosen so that the scaled NMR relaxation rates agree with the μSR rates at high T where no field dependence is observed. After this scaling, we find a good agreement between the μSR and NMR data at all temperatures at *the same external field*, and not equal Larmor frequency of the probe as one would expect, this result will be clarified in section 5.3.

The scaling factor provides information on the ratio of the field experienced by a muon and by a proton. At high temperatures where T_1 shows no field dependence one can assume that $A \gg BH^2$ in Eq. (4.5), and therefore $1/T_1 = \Delta^2\tau$. Using the definition of Δ^2 given in Eq. (4.8) we can write

$$C \equiv \left(\frac{\gamma_H}{\gamma_\mu}\right)^2 \left(\frac{T_1^H}{T_1^\mu}\right) = \frac{\langle B_\perp^2 \rangle^\mu}{\langle B_\perp^2 \rangle^H} \tag{4.25}$$

where $\langle B_\perp^2 \rangle^H$ is the squared RMS of the transverse field at the proton site, and $\langle B_\perp^2 \rangle^\mu$ is the squared RMS of the field at the muon site in its general sense given by Eq. (4.9).

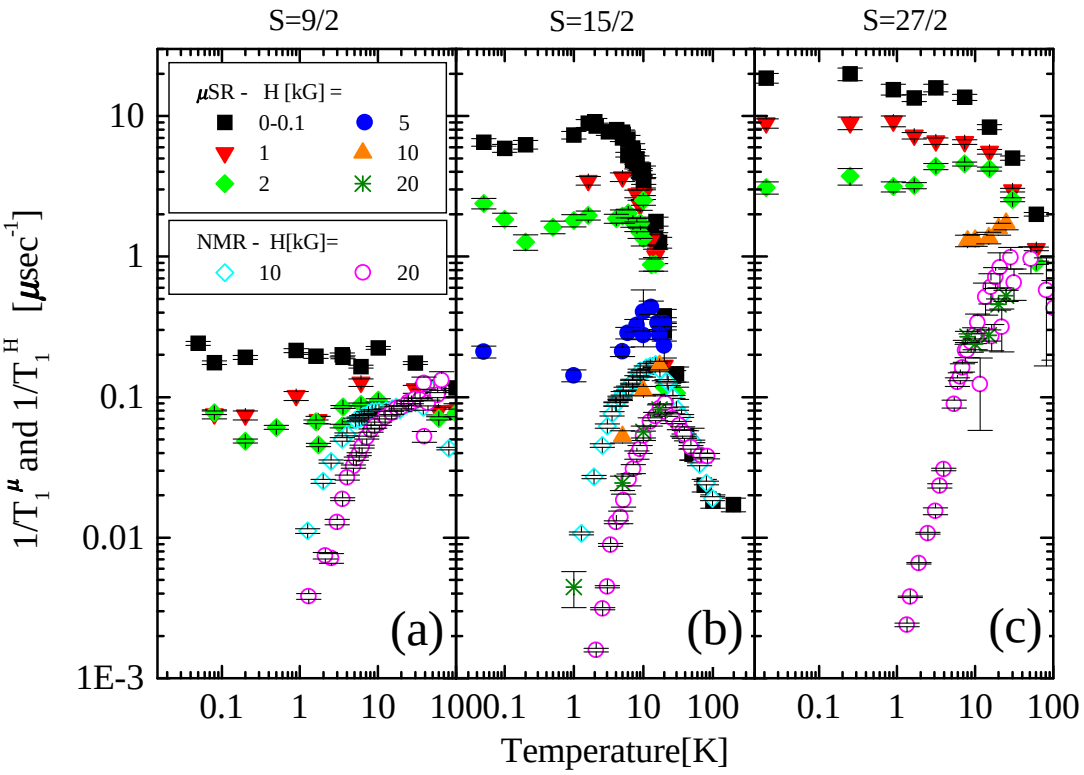

Figure 4.30: $1/T_1$ as a function of temperatures for different external fields, measured by μSR and by NMR (after scaling) in (a) $CrCu_6$ (b) $CrNi_6$ and (b) $CrMn_6$.

The values of C indicate that the local field experienced by the muons is of the order of 0.1 of that experienced by protons in the same system, and therefore the muon sites are far from the magnetic ions compared to protons.

Muons are attracted to negatively charged sites, in the HSM two negatively charged sites are possible

- The cyanide bridge connecting the central Cr ion to the Cu, Ni or Mn ions.
- The perchlorate group separating the molecules.

The distance of each of these sites is much larger than the distance between the hydrogen atoms and magnetic ions. This fact is consistent with the ratio of the magnetic field experienced by muons to that experienced by protons.

This comparison indicates strongly that in both techniques we are measuring the probe's spin lattice relaxation time due to the molecular spin fluctuations.

4.6 Summary

The μSR measurements in anisotropic Fe_8 ($S = 10$) molecules show that the local magnetic field experienced by muons in this compound is static over the lifetime of muons. QTM is seen through steps in the local magnetic field experienced by muons as a function of the field cycle applied on the compound before performing the measurement.

In the isotropic HSM no QTM is found, due to the lack of an anisotropy barrier between the different spin states. The local field experienced by the muons in these compounds is dynamically fluctuating down to very low temperatures ($T = 50$ mK), and the muon's spin relaxes via spin-lattice relaxation, enabling us to measure the fluctuations rate of the molecular spin.

Spin-lattice relaxation values measured by proton-NMR in isotropic HSM scale with those measured using μSR at the same external field, supporting the assumption that the muon's spin relaxes due to field fluctuations and not muon diffusion, and furthermore it exhibit the isotropic nature of these molecules.

The spin-lattice relaxation in the isotropic HSM was compared to that measured in the paramagnet Gd ($S = 7/2$). The muon spin-lattice relaxation rate in Gd was found to be temperature independent at all measured temperatures (50 mK up to

300 K), and no field dependence was observed.

A temperature independent spin lattice relaxation rate was found in all isotropic HSM at low temperatures and low fields similar to that observed in the Gd compound, indicating again the isotropic nature of the HSM. However, external field dependence of the muon spin lattice relaxation was absent in Gd (up to 2 kG), while strong field dependence was found in the isotropic HSM.

The molecular spin fluctuations rate in the isotropic HSM was calculated from the field dependence of the muon spin lattice relaxation rate at low temperatures and low fields. It was found to depend weakly on the molecular spin S and the coupling between ions' spins inside the molecule J, ruling out fluctuations that are induced by interactions which depend strongly on these parameters.

Chapter 5

Theoretical Calculations

The Hamiltonian of the isotropic high spin molecules at zero field can be written as

$$\mathcal{H}_0 = -J \sum_{i=1}^{6} \vec{S}_0 \cdot \vec{S}_i \tag{5.1}$$

where $\vec{S}_0$ is the spin of the central Cr ion (with $S = 3/2$), i runs over the peripheral Cu, Ni or Mn ions (with $S = 1/2$, $S = 1$ or $S = 5/2$), which are coupled to the central Cr ion, with coupling constant J. At temperatures lower than J only the ground spin state $S = 9/2$, $S = 15/2$ or $S = 27/2$ is populated.

The Hamiltonian $\mathcal{H}_0$ is isotropic therefore the total spin S and the spin in the z direction m are good quantum numbers, and the eigenfunctions of $\mathcal{H}_0$ can be written as $|S, m>$. However, at very low temperatures $T \ll J$, the degeneracy of the ground state is removed by additional anisotropic perturbation on $\mathcal{H}_0$ or high order terms in the spin Hamiltonian. Such terms that do not commute with $\mathcal{H}_0$ can cause transitions between the different spin states $|S, m>$ [27, 28, 29, 30, 31, 40, 41, 64, 65, 66, 67], and induce the observed spin dynamics.

The anisotropic term in the Hamiltonian can be written as the sum $\mathcal{H}' = \mathcal{H}_c + \mathcal{H}_n$, where $\mathcal{H}_c$ commutes with the Hamiltonian $\mathcal{H}_0$, and $\mathcal{H}_n$ does not commute with it.

These terms may be a result of to dipolar interaction between neighboring spins [27, 66], spin phonon interaction [40, 67], nuclear fluctuations [41], high order crystal field terms [4, 27, 28, 29, 30, 31] or small anisotropy in the coupling J between spins [68].

In this chapter we will calculate the value of the spin lattice relaxation time T_1 in the isotropic HSM. In order to do that we diagonalize the Hamiltonian $\mathcal{H}_0 + \mathcal{H}_c$. We show that we can calculate the magnetization and susceptibility of the compounds using the eigenvalues and eigenfunctions that we obtain. Then we use the eigenvalues and eigenfunctions of the Hamiltonian to calculate T_1, taking $\mathcal{H}_n$ as a perturbation. The perturbation introduces a finite lifetime for the different spin states $|S, m>$ and induces spin dynamics.

5.1 Exact diagonalization of the Hamiltonian

To calculate the eigenvalues of the Hamiltonian (5.1) we write it in the form

$$\mathcal{H}_0 = -J\vec{S}_0 \cdot \sum_{i=1}^{6} \vec{S}_i \tag{5.2}$$

using $\vec{S} = \vec{S}_0 + \sum_{i=1}^{6} \vec{S}_i$ and $\vec{S}_t = \sum_{i=1}^{6} \vec{S}_i$ one can write

$$\mathcal{H}_0 = -J\vec{S}_0 \cdot \vec{S}_t = -\frac{J}{2}\left(\vec{S}^2 - \vec{S}_t^2 - \vec{S}_0^2\right). \tag{5.3}$$

The energy eigenvalues of the sates $|S, m> \equiv |S_0, S_t, S, m>$ are

$$E_{\mathbf{S}} \equiv E(S, S_t, S_0) = -\frac{J}{2}\left(S(S+1) - S_t(S_t+1) - S_0(S_0+1)\right) \tag{5.4}$$

where we use the notation $\mathbf{S}$ for the set of numbers (S, S_t, S_0). The degeneracy of the state $|S, m>$ is the degeneracy of the value of S_t. In Figure 5.1 we present the

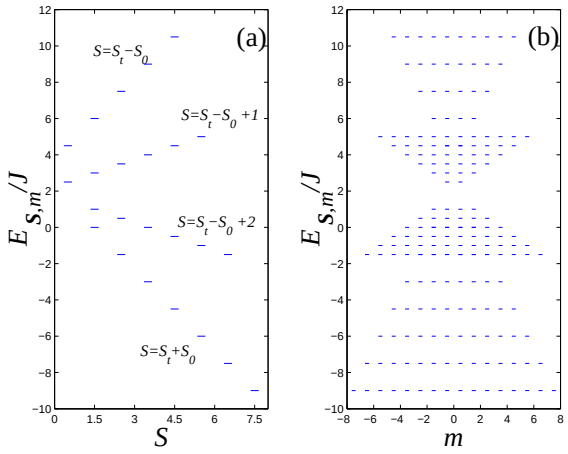

Figure 5.1: The energy levels of the Hamiltonian $\mathcal{H}_0$ for $CrNi_6$ as a function of (a) the total spin S and (b) the spin in the z direction m.

energy levels of $CrNi_6$ as a function of the total spin S (a) and as a function of the spin in z direction m (b).

Adding the Zeeman term when an external magnetic field H is applied and the uniaxial term with anisotropy D to the Hamiltonian $\mathcal{H}_0$ gives the full Hamiltonian

$$\mathcal{H} = \mathcal{H}_0 - g\mu_B H S_z - D S_z^2 \tag{5.5}$$

for which the eigenfunctions $|S, m>$ are not changed and the eigenvalues are

$$E_{\mathbf{S},m} = -\frac{J}{2}\left(S(S+1) - S_t(S_t+1) - S_0(S_0+1)\right) - g\mu_B H m - D m^2 \tag{5.6}$$

5.2 Static susceptibility

The static susceptibility can be calculated as a function of temperature and external field, first we calculate the magnetization

$$M(T) = < S_z > = \sum_{|S,m>} \frac{m e^{-\frac{E_{\mathbf{S},m}}{T}}}{\mathcal{Z}} \tag{5.7}$$

where $\mathcal{Z} = \sum_{|S,m>} \exp\left(-\frac{E_{\mathbf{S},m}}{T}\right)$ is the partition function. The static susceptibility is defined as $\chi = \partial M/\partial H$. However at low fields where M is proportional to H the susceptibility is equal to its "experimental definition"

$$\chi(T) = \frac{M(T)}{H}. \tag{5.8}$$

In Figure 5.2 we fit the experimental measurement of χT as a function of temperature in (a) $CrCu_6$, (b) $CrNi_6$ and (c) $CrMn_6$, at fields $H = 100$ G and 2.15 T, to the calculated value of χT from the Hamiltonian (5.5) and Eq. (5.8). From the fit one obtains the coupling constants $J_{\mathrm{Cr-Cu}} = 77$ K, $J_{\mathrm{Cr-Ni}} = 24$ K and $J_{\mathrm{Cr-Mn}} = -11$ K and anisotropy $D \simeq 0$ for all three molecules, within the fitting accuracy. This

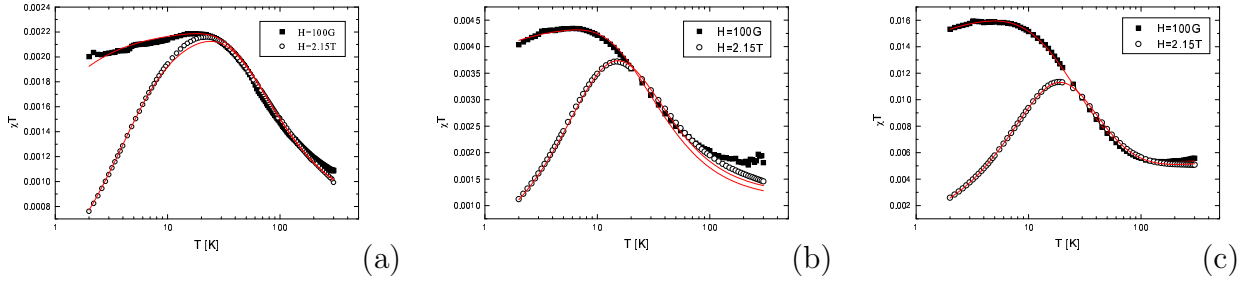

Figure 5.2: The susceptibility multiplied by temperature as a function of temperature at two different external fields, measured in (a) $CrCu_6$ (b) $CrNi_6$ and (c) $CrMn_6$. The solid lines are fits to the theoretical expectation (see text).

indicates that indeed the high spin molecules can be well described by the Hamiltonian (5.5), and that the molecules are indeed isotropic.

5.3 T_1 Calculation

Assuming for simplicity an isotropic interaction between the probe $\vec{I}$ and the local electronic spins $\vec{S}$

$$\mathcal{H}_{IS} = A\vec{I}\cdot\vec{S} \tag{5.9}$$

the spin lattice relaxation is given by [63]

$$\frac{1}{T_1} = \frac{A^2}{2}\int_{-\infty}^{\infty} \langle S_-(t)S_+(0)\rangle\, e^{i\omega t}dt \tag{5.10}$$

where $\omega = \gamma H$ is the probe's Larmor frequency in an external field H. To calculate the value of

$$\langle S_-(t)S_+(0)\rangle = \left\langle e^{-i\mathcal{H}t/\hbar}S_-e^{i\mathcal{H}t/\hbar}S_+\right\rangle \tag{5.11}$$

for the eigenstates $|S,m>$ of (5.5), we start by evaluating

$$\begin{aligned} e^{-i\mathcal{H}_0t/\hbar}S_-e^{i\mathcal{H}_0t/\hbar}S_+|S,m> &= e^{-i\mathcal{H}_0t/\hbar}S_-e^{i\mathcal{H}_0t/\hbar}\sqrt{S(S+1)-m(m+1)}|S,m+1> \\ &= (S(S+1)-m(m+1))\, e^{i\left(\frac{E_{\mathbf{S},m+1}-E_{\mathbf{S},m}}{\hbar}\right)t}|S,m> \end{aligned}$$

therefore

$$\langle S_-(t)S_+(0)\rangle = \sum_{|S,m>}(S(S+1)-m(m+1))\, e^{i\left(\frac{E_{\mathbf{S},m+1}-E_{\mathbf{S},m}}{\hbar}\right)t}\frac{e^{-\frac{E_{\mathbf{S},m}}{T}}}{\mathcal{Z}} \tag{5.12}$$

where $\mathcal{Z}$ is the partition function, this yields

$$\frac{1}{T_1} = \frac{A^2}{2}\delta\left(\omega + \frac{E_{\mathbf{S},m+1}-E_{\mathbf{S},m}}{\hbar}\right)\sum_{|S,m>}\frac{e^{-\frac{E_{\mathbf{S},m}}{T}}}{\mathcal{Z}}\left(S(S+1)-m(m+1)\right). \tag{5.13}$$

This result is true for a system with levels of infinitely long lifetime. However, assuming a Lorentzian broadening of the levels, due to the non-commuting additional terms in the Hamiltonian $\mathcal{H}_n$, we arrive at

$$\langle S_-(t)S_+(0)\rangle = \sum_{|S,m>}\frac{e^{-\frac{E_{\mathbf{S},m}}{T}}}{\mathcal{Z}}\left(S(S+1)-m(m+1)\right)e^{-\frac{t}{\tau_{S,m}}}e^{i\left(\frac{E_{\mathbf{S},m+1}-E_{\mathbf{S},m}}{\hbar}\right)t} \tag{5.14}$$

where $\tau_{S,m}$ is the lifetime (or the inverse of the broadening) of the level $E_{\mathbf{S},m}$. Hence

$$\frac{1}{T_1} = \frac{A^2}{2} \sum_{|S,m>} \frac{e^{-\frac{E_{\mathbf{S},m}}{T}}}{\mathcal{Z}} \left(S(S+1) - m(m+1)\right) \int_{-\infty}^{\infty} e^{-\frac{t}{\tau_{S,m}}} e^{i\omega' t} dt \tag{5.15}$$

where $\omega' = \omega + (E_{\mathbf{S},m+1} - E_{\mathbf{S},m})/\hbar$. The energy eigenvalues of the Hamiltonian (5.5) are total spin independent, in our case of isotropic molecules $D = 0$, and the energy difference is $E_{\mathbf{S},m+1} - E_{\mathbf{S},m} \simeq -g\mu_B H$, therefore $\omega' = \omega - \frac{g\mu_B}{\hbar} H$ and

$$\frac{1}{T_1} = \frac{A^2}{2\mathcal{Z}} \sum_{|S,m>} \left(S(S+1) - m(m+1)\right) \left(\frac{\tau_{S,m} e^{-\frac{E_{\mathbf{S},m}}{T}}}{1 + \omega'^2 \tau_{S,m}^2} \right). \tag{5.16}$$

This result gives an important understanding of the comparison between the spin lattice relaxation rate measured by μSR and NMR. The field dependence of $1/T_1$ comes from $\omega' = (\gamma - g\mu_B/\hbar)H$. Since the gyromagnetic ratio γ of the probe (muon or nucleus) is much smaller than $g\mu_B/\hbar$ (electronic gyromagnetic ratio), $\omega' \simeq -g\mu_B H/\hbar$ does not depend on the value of γ. Therefore the field dependence of the spin lattice relaxation rate $1/T_1$ is independent of the value of γ. This explains the fact that the spin lattice relaxation rate measured by proton-NMR can be scaled to match that measured by μSR *at the same external field*, and not at the same Larmor frequency of the probe. However, Eq. (5.16) is valid assuming that $\mathcal{H}_n$ is smaller than the Zeeman splitting, $E_{\mathbf{S},m+1} - E_{\mathbf{S},m}$, i.e. at high fields $g\mu_B H \gg \mathcal{H}_n$. When the Zeeman splitting is smaller than $\mathcal{H}_n$, ω' should be replaced by $\omega = \gamma H$, in Eq. (5.16).

The lifetime $\tau_{S,m}$ of the level $|S, m>$ can be expressed in terms of transition probability from the state $|S, m>$ to another state $|S', m'>$

$$\frac{1}{\tau_{S,m}} = \sum_{(S',m') \neq (S,m)} p(S, m \rightarrow S', m') \tag{5.17}$$

which depends on the additional parts of the Hamiltonian that induce these transitions. I will try to account for this lifetime assuming different possible interactions.

5.3.1 Spin-Phonon Interaction

To account for the temperature dependence of T_1 we should take into consideration the transitions induced by spin-phonon interactions. The spin-phonon coupling Hamiltonian [67, 69] of the ion n is

$$\mathcal{H}_{sp}^{n} = \sum_{\alpha} g_{ijkl}\omega_{\alpha}^{-1/2} e_{\alpha i} q_{\alpha j}(a_{\alpha} + a_{\alpha}^{\dagger})(S_k^n S_l^n + S_l^n S_k^n) \tag{5.18}$$

where α labels the phonon modes with annihilation creation operators a_α and $a_\alpha^\dagger$, q_α, e_α and ω_α are the wave vector, polarization and frequency, respectively. i, j, etc. are Cartesian indices. For the sake of simplicity we assume that the tensor g_{ijkl} is only weakly q dependent.

The Hamiltonian (5.18) holds for an individual spin of an ion inside the molecule, i.e. a phonon can interact with an individual spin of an ion causing a change in the ion's spin and a transition of the spin state of the whole molecule. The total spin-phonon Hamiltonian of the whole molecule is the sum of all the individual ions' Hamiltonians

$$\mathcal{H}_{sp} = \sum_{n} \mathcal{H}_{sp}^{n} \tag{5.19}$$

Assuming that the coupling constant in the Hamiltonian (5.18) is constant, and independent of the ion n, one can write the transition rate from a state $|S, m>$ to a state $|S', m'>$, using the golden rule in perturbation theory [70]

$$p(S, m \to S', m') = \frac{3}{2\pi} \frac{|\langle S, m|\mathcal{H}_{sp}|S', m'\rangle|^2}{\hbar^4 \rho c^5} (E_{\mathbf{S},m} - E_{\mathbf{S}',m'})^3 \frac{1}{\exp\left[(E_{\mathbf{S},m} - E_{S',m'})/T\right] - 1} \tag{5.20}$$

This result involves the matrix element $\langle S, m|\mathcal{H}_{sp}|S', m'\rangle$ of the spin phonon interaction, the phonon velocity c, the specific mass ρ and the energy difference $(E_{\mathbf{S},m} - E_{\mathbf{S}',m'})$, where it was assumed that $E_{\mathbf{S},m} > E_{\mathbf{S}',m'}$. To get the right order of magnitude, and simplify the calculations, we assume a constant spin phonon interaction

matrix element, arriving at

$$p(S,m \to S',m') = \frac{C(E_{\mathbf{S},m} - E_{\mathbf{S}',m'})^3}{\exp\left[(E_{\mathbf{S},m} - E_{\mathbf{S}',m'})/T\right] - 1} \tag{5.21}$$

where

$$C = \frac{3}{2\pi} \frac{|\langle S,m|\mathcal{H}_{sp}|S',m'\rangle|^2}{\hbar^4 \rho c^5}.$$

The transition probability due to spin-phonon interaction strongly depends on temperature. At very low temperature phonons die out exponentially with decreasing temperature, yielding a very low transition probability, and extremely low spin lattice relaxation rate values $1/T_1$ as seen in Figure 5.3. Therefore this interaction cannot give a full explanation to the nonzero spin lattice relaxation rate at low temperatures, which is observed in experiments [64, 65], and additional terms in the Hamiltonian should be considered.

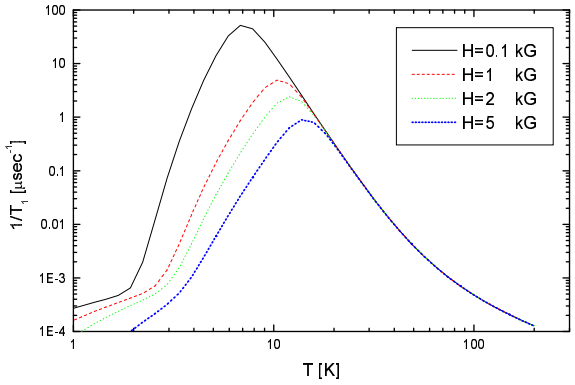

Figure 5.3: Spin lattice relaxation rate as a function of temperature for different fields in $CrNi_6$, when assuming spin-phonon interactions only, where $C = 400$ 1/sec K^3 and $A = 5.2$ MHz.

5.3.2 Other Interactions

In order to obtain a finite spin lattice relaxation rate at very low temperatures, the lifetime of the levels should be finite. This cannot be accounted for by spin-phonon interaction as seen in the previous section. A finite lifetime can be achieved if one simply assumes a finite broadening of the levels due to an additional interaction $\mathcal{H}_{int}$, giving a short lifetime τ_{int} for the levels. The assumption implied by the experimental results [65] is that τ_{int} is temperature and field independent at low fields.

In this case the total lifetime of the levels is

$$\frac{1}{\tau_{S,m}} = \left(\frac{1}{\tau_{sp}} + \frac{1}{\tau_{int}}\right). \tag{5.22}$$

At high temperatures the value of the spin-phonon contribution to the lifetime, τ_{sp}, is much smaller than τ_{int} and the value of T_1 is dominated by spin-phonon induced transitions, while at very low temperatures τ_{sp} is much longer than τ_{int}, and the value of T_1 is dominated by the broadening of the levels (or τ_{int}). At intermediate temperatures both mechanisms contribute to the spin lattice relaxation.

In Figure 5.4 we present the experimental values of $1/T_1$, measured by μSR [65], as a function of temperature at different fields, for the molecules (a) $CrCu_6$, (b) $CrNi_6$, and (c) $CrMn_6$. The solid lines are fits to the theoretical value expected assuming transitions which are induced by spin-phonon interaction in addition to a finite broadening of the levels, as described above. The fits give the values summarized in Table 5.1.

The values of τ_{int} obtained from the fits are much smaller than those calculated form the experimental results τ_0 in section 4.2. The values τ_{int} were calculated using Eq. (5.16) with $\omega' \simeq g\mu_B H$, while the calculation in section 4.2 assumes that

$$\frac{1}{T_1} = \frac{\Delta_0^{*2}\tau_0}{1+\omega^2\tau_0^2}. \tag{5.23}$$

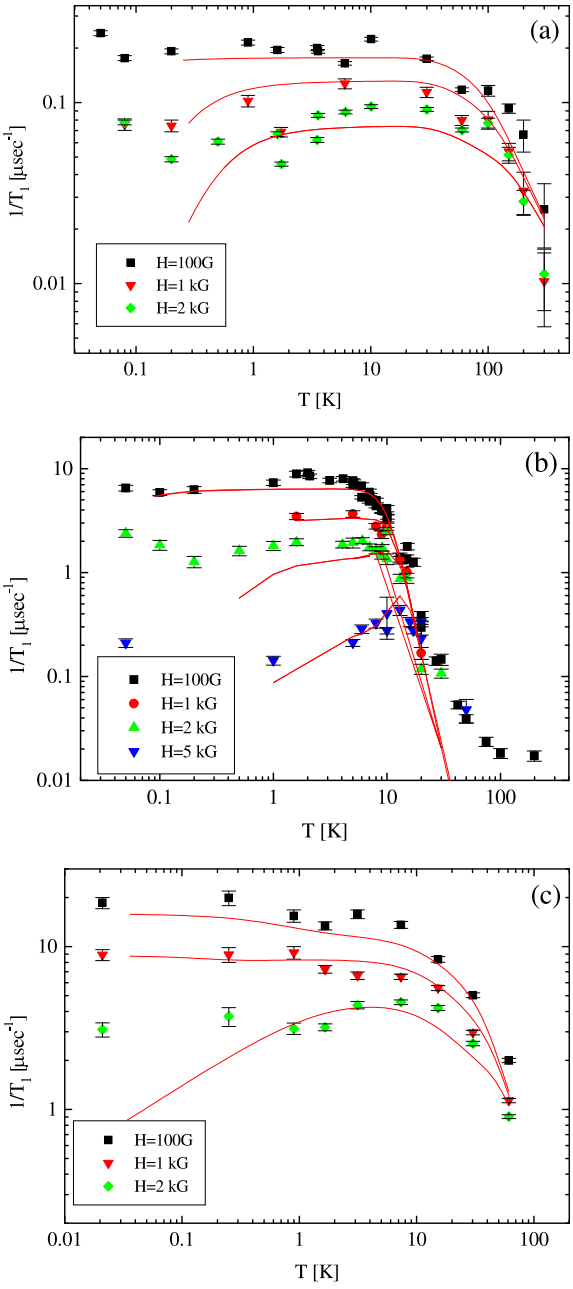

Figure 5.4: The value of $1/T_1$ as a function of T at different fields, measured using μSR in (a) $CrCu_6$, (b) $CrNi_6$ and (c) $CrMn_6$. The solid lines are fits to the calculated value (see text).

Compound	τ_{int} [nsec]	C [1/sec K^3]	A [MHz]
$CrCu_6$	0.034(4)	0.13(9)	1.7(1)
$CrNi_6$	0.053(4)	400(60)	5.2(2)
$CrMn_6$	0.044(4)	0.004(1)	4.7(2)

Table 5.1: The fit parameters of the theoretical calculation of the spin lattice relaxation to the experimental values from μSR measurements

where $\omega = \gamma_\mu H$. Therefore we expect that the relation between τ_0 and τ_{int} follows

$$\frac{\tau_0}{\tau_{int}} = \frac{\omega'}{\omega} \simeq \frac{g\mu_B}{\gamma_\mu}. \tag{5.24}$$

For a muon we expect $\tau_0/\tau_{int} = 206.5$ which is indeed the ratio of the values from Tables 5.1 and 4.1. Similarly the values of Δ^* from Table 4.1 are related to the values of A from Table 5.1 by

$$\Delta^* = \frac{AS}{\sqrt{2}} \tag{5.25}$$

which hold within the error for all three molecules.

The values of τ_{int} is Table 5.1 indicate that $\mathcal{H}_n$ is of order of $0.7 - 1.1$ K, which is larger than the Zeeman splitting in fields up to 2 kG. Therefore to get the right values of τ_{int} one should use Eq. (5.16) with $\omega = \gamma_\mu H$ instead of ω'. This yeilds values of τ_{int} as follows: $\tau_{int} = 7.0(8)$ nsec for $CrCu_6$, $\tau_{int} = 10.9(8)$ nsec for $CrNi_6$, and $\tau_{int} = 9.1(8)$ nsec for $CrMn_6$.

The fits in Figure 5.4 are satisfactory, considering the simplifications that we have used, and it gives the correct general behavior of the experimental data. However, at very low temperatures and high fields the theoretical calculation deviates from the experimental data. Similarly at high temperatures $T \gg J$, where $1/T_1$ is very small, the theoretical calculation deviates from the experimental data (especially in the case of $CrNi_6$). We believe that the origins of the deviation at high temperatures is that

the Hamiltonian (5.5) does not describe the system well enough, and that the value of $1/T_1$ is very small and is harder to estimate experimentally. This can also be seen in Figure 5.2, where at high temperatures the calculated value of χT deviates from the experimental values.

5.4 Summary

The calculated spin lattice relaxation rate of a local probe, with gyromagnetic ratio γ, in the isotropic HSM follows Eq. (5.16). This result remains valid assuming an isotropic interaction between the probe's spin and the molecular spin, and assuming a finite lifetime $\tau_{S,m}$ for the spin state $|S, m >$.

Eq. (5.16) indicates that the spin lattice relaxation rate in these molecules is almost independent of the probe's gyromagnetic ratio, and therefore the measured values of spin lattice relaxation by μSR and proton-NMR scale at the same external field, and not at equal Larmor frequencies.

The parameters deduced from the fit of the experimental results to Eq. (5.16) agree with the calculated local field Δ^* experienced by muons, and with the calculated fluctuations rate τ_0 calculated by μSR.

The lifetime $\tau_{S,m}$ of the spin state $|S, m >$ is dominated by two mechanisms, the first is spin phonon interaction (thermal activation) which dominates the high temperature regime $T \gg J$, and the second is a temperature and field independent interaction which dominates the low temperature regime $T \ll J$. The interaction which dominates the spin lattice relaxation at low temperatures and low fields, was found to depend weakly on the value of S and J.

Chapter 6

Conclusions

Using the μSR technique we observed quantum tunneling of the magnetization (QTM) in Fe_8 ($S = 10$) compound. We sweep the external magnetic field applied on the Fe_8 sample from +2 T, to some intermediate field H_i, and then to -50 G at $T = 40$ mK where no thermal activation occurs. The precession frequency of muons in the sample changes depending on the value of H_i. QTM is observed through steps in the frequency as a function of H_i, which reflects tunneling between different spin states of the neighboring Fe_8 molecules. These steps coincide with the matching fields, at which different molecular spin states of different directions, up or down, have the same energy level, and therefore the molecular spin can tunnel between them.

In the high spin molecules (HSM) $CrCu_6$ ($S = 9/2$), $CrNi_6$ ($S = 15/2$) and $CrMn_6$ ($S = 27/2$) no evidence of QTM is found, this is due to the fact that these molecules are highly isotropic. The results from magnetic measurements indicate that the main part of spin Hamiltonian for these molecules is of the form

$$\mathcal{H} = -J \sum_{i=1}^{6} \vec{S}_0 \cdot \vec{S}_i - g\mu_B \vec{H} \cdot \sum_{i=0}^{6} \vec{S}_i \tag{6.1}$$

where $\vec{S}_0$ is the spin on the central Cr ion and $\vec{S}_i$ are the spins of the Cu, Ni or Mn

ions. $\vec{H}$ is the external magnetic field and J is the coupling between the spins of the Cr ion with each one of the Cu, Ni or Mn ions. The values of the coupling are found to be $J_{\mathrm{Cr-Cu}} \approx 77$ K, $J_{\mathrm{Cr-Ni}} \approx 24K$ K and $J_{\mathrm{Cr-Mn}} \approx -11$ K. In such isotropic HSM any small perturbation added to the Hamiltonian (6.1) can drive transitions between the different spin states, even at very low temperatures.

We studied the dynamics of the molecular spins of the isotropic molecules through spin lattice relaxation measurements using μSR and NMR. The spin lattice relaxation rate is closely related to the local field time correlation function in the site of the measurement probe (muon or nucleus). It is found that in the isotropic HSM the spin lattice relaxation rate increases when decreasing the temperature, and saturates at low temperatures $T \ll J$, and low fields.

When comparing the spin lattice relaxation rate in the isotropic HSM with that measured in the high spin paramagnetic compound Gd ($S = 7/2$), the fact that the molecules $CrCu_6$, $CrNi_6$, and $CrMn_6$ are indeed isotropic, is again proven. The spin lattice relaxation in Gd is found to be temperature independent at all temperatures due to the fact that it is a paramagnet that has no significant energy scale at zero field, similar to what is seen in the isotropic HSM at low temperatures.

Assuming an isotropic interaction between the local probe (with gyromagnetic ratio γ) and the molecular spin, and that the lifetime of the spin states $|S, m>$ is $\tau_{S,m}$, one can write the spin lattice relaxation rate in the isotropic HSM in the form

$$\frac{1}{T_1} = \frac{A^2}{2\mathcal{Z}} \sum_{|S,m>} (S(S+1) - m(m+1)) \left(\frac{\tau_{S,m} e^{-\frac{E_{\mathbf{S},m}}{T}}}{1 + \omega'^2 \tau_{S,m}^2} \right) \tag{6.2}$$

where A is the coupling constant between the molecular and probe spins, $E_{\mathbf{S},m}$ is energy of the state $|S, m>$, $\omega' = \omega - \frac{g\mu_B}{\hbar} H$ with ω the Larmor frequency of the probe in field H, and $\mathcal{Z}$ is the partition function.

In order to fit the calculated value of $1/T_1$ to the experimental results from μSR, one has to take into consideration two contributions to the life time of the levels

$$\frac{1}{\tau_{S,m}} = \left(\frac{1}{\tau_{sp}} + \frac{1}{\tau_{int}}\right) \tag{6.3}$$

where τ_{sp} is the contribution from spin-phonon interaction

$$\frac{1}{\tau_{sp}} = \sum_{|S',m'>} \frac{C(E_{\mathbf{S},m} - E_{\mathbf{S}',m'})^3}{\exp\left[(E_{\mathbf{S},m} - E_{\mathbf{S}',m'})/T\right] - 1} \tag{6.4}$$

and τ_{int} is a constant, which is contributed by an additional interaction. At high temperatures $T \gg J$, we have $\tau_{sp} \ll \tau_{int}$ and the lifetime of the levels is dominated by spin-phonon interaction, yielding $\tau_{S,m} \simeq \tau_{sp}$, while at low temperatures $T \ll J$, we have $\tau_{sp} \gg \tau_{int}$ and the lifetime is dominated by the additional interaction, yielding $\tau_{S,m} \simeq \tau_{int}$.

Thus the spin dynamics in the high temperature regime is governed by thermal activation, i.e. the probe's spin lattice relaxation is dominated by transitions between the different electronic spin states $|S, m>$ with different S value, which are thermally activated. Once the temperature is low and only the $2S+1$ degenerate electronic spin ground state is populated, transitions due to thermal activation between different S states become scarce and spin dynamics is solely due to transitions between states with different m value.

The calculated lifetime of the levels τ_{int} is found to vary between $7 - 11$ nsec, which can be translated to a broadening of $3 - 5$ mK. Therefore we expect that the interaction which introduces the spin dynamics in these molecules produces level broadening of the same order of magnitude.

The temperature and field independent levels broadening $1/\tau_{int}$ calculated above can be attributed to an interaction that does not commute with S_z and induces

transitions between the different m states. This interaction can be dipolar between neighboring molecules, hyperfine between molecular and nuclear spins, crystal field higher order terms, etc. However, the striking fact is that the lifetime is similar in all three molecules, indicating that it does not depend strongly on the spin of the molecule or the coupling J between ions inside the molecule, which varies greatly between the three molecules.

This indicates that the weak dependence of the broadening on the spin value cannot be explained by interactions which are quadratic in S or have higher S dependence. This rules out dipolar interactions between neighboring molecules since in the three compounds the nearest neighbor distance is ~ 15 Å. Similarly, crystal field terms which are allowed by the octahedral symmetry (S^2 or higher [71]) are unlikely.

The only mechanism suggested to date for level broadening of HSM, which depends weakly on S is the hyperfine interaction between nuclear and electronic spins. This mechanism can account for the finite spin lattice relaxation rate at very low temperatures [72]. However, the values of broadening calculated above might be inaccurate due to the simplifications made in the calculations, but give the right order of magnitude expected from hyperfine interactions [73].

Hyperfine interactions in anisotropic high spin molecules were studied recently [31, 47], and their effect on QTM is becoming clearer [74, 75]. We believe that this interaction also governs the spin dynamics of the isotropic molecules at very low temperatures ($T < 3$ K), while at high temperature ($T > 10$ K) the molecular spin dynamics are governed by spin-phonon interactions.

References

[1] J. Harris and D. Awschalom. *Physics World*, 1999.

[2] N. Prokofév and P. Stamp. *J. Low Temp. Phys.*, 104:143, 1996.

[3] J. Tejada J. Freidman, M. Sarachik and R. Ziolo. *Phys. Rev. Lett.*, 76:3830, 1996.

[4] C. Sangregorio T. Ohm C. Paulsen R. Sessoli and D. Gateschi. *Phys. Rev. Lett.*, 78:4645, 1997.

[5] J. Hernández X. Zhang F. Luis J. Bartolomé. J. Tejada and R. Ziolo. *Europhys. Lett.*, 35:301, 1996.

[6] A. Keren. PhD thesis, Colombia University, 1994.

[7] J. Tejada X. Zhang and E. Chudnovsky. *Phys. Rev. B*, 47:14977, 1993.

[8] J. Tejada, L. Balcells. S. Linderoth R. Perzynski B. Rigau B. Barbara J. C. Bacri. *J. Appl. Phys.*, 73:6952, 1993.

[9] X. X. Zhang J. Tejada. *J. Appl. Phys.*, 75:5642, 1994.

[10] B. Barbara L. C. Sampaio J. E. Wegrowe B. A. Ratnam A. Marchand C. Paulsen M. A. Novak J. L. Tholence M. Uehara and D. Fruchart. *J. Appl. Phys.*, 73:6703, 1993.

[11] C. Paulsen and J. Park. In L. Gunther and B. Barbara, editors, *Quantum Tunneling of the Magnetization - QTM '94*, page 189. Kluwe Publishing, Dordrecht, 1995.

[12] D. Divincenzo. In L. Gunther and B. Barbara, editors, *Quantum Tunneling of the Magnetization - QTM '94*, page 189. Kluwe Publishing, Dordrecht, 1995.

[13] T. Lis. *Acta Crystallogr. Sec. B*, 36:2042, 1980.

[14] A. Caneschi D. Gatteschi R. Sessoli A. L. Barra L. C. Brunel and M. Guillot. *J. Am. Chem. Soc.*, 113:5873, 1991.

[15] R. Sessoli H. L. Tsai A. R. Schake S. Wang J. B. Vincent K. Folting D. Gatteschi G. Christou and D. N. Hendrickson. *J. Am. Chem. Soc.*, 115:1804, 1993.

[16] M. A. Novak R. Sessoli A. Caneschi and D. Gatteschi. *JMMM*, 146:211, 1995.

[17] K. Wieghardt K. Pohl I. Jibril and G. Huttner. *Angew. Chem. Int. Ed. Engl.*, 23:77, 1984.

[18] I. Mirebeau M. Hennion H. Casalta H. Andres H. U. Güdel A. V. Irodova and A. Caneschi. *Phys. Rev. Lett.*, 83:628, 1999.

[19] K. M. Mertes M. P. Srachik Y. Paltiel H. Shtrikman E. Zeldov E. M. Rumberger and D. N. Hendrickson. *cond-mat 0108185*, 2001.

[20] L. Thomas F. Lionti R. Ballou D. Gatteschi R.Sessoli and B. Barbara. *Letters to Nature*, 383:145, 1996.

[21] A. Barra P. Debrunner D. Gateschi C. Schulz and R. Sessoli. *Europhys. Lett.*, 35:133, 1996.

[22] M. Novak and R. Sessoli. In L. Gunther and B. Barbara, editors, *Quantum Tunneling of the Magnetization - QTM '94*, page 189. Kluwe Publishing, Dordrecht, 1995.

[23] T. Mallah S. Ferlay A. Scuillier M. Verdaguer. In O.Kahn, editor, *Proceedings of the NATO ARW, Molecular Magnetism: a Supramolecular Function*, page 594. Kluwer Academic publishers, 1996.

[24] A. Scuiller T. Mallah A. Nivorozkhin M. Verdaguer P. Veillet. *New J. Chem.*, 20:1, 1996.

[25] V. Marvaud C. Decroix A. Scuiller J. Vaissermann C. Guyard F. Gonnet M. Verdaguer. 2001.

[26] T. Mallah C. Auberger M. Verdaguer and P. Veillet. *J. Chem Soc., Chem. Commun.*, 1:61, 1995.

[27] P. Politi A. Retori F. Hartmann-Boutron and J. Vilain. *Phys. Rev. Lett.*, 75:537, 1995.

[28] D. Gatteschi A. L. Barra and R. Sessoli. *Phys. Rev. B*, 56:8192, 1997.

[29] A. Barra A. Caneschi D. Gatteschi and R. Sessoli. *JMMM*, 177, 1998.

[30] A. Fort A. Rettori J. Villain-D. Gatteschi and R. Sessoli. *Phys. Rev. Lett.*, 80:612, 1998.

[31] A. Caneschi T. Ohm D. Rovai-C. Sangregorio and R. Sessoli. *JMMM*, 177, 1998.

[32] J. L. van Hemmen and A. Suëtö. *Europhys. Lett.*, 1:481, 1986.

[33] J. L. van Hemmen and A. Sütö. In L. Gunther and B. Barbara, editors, *Quantum Tunneling of the Magnetization - QTM '94*, page 19. Kluwe Publishing, Dordrecht, 1995.

[34] J. Hernandéz X. Zhang F. Luis and J. Tejada. *Phys. Rev. B*, 55:5858, 1997.

[35] D. A. Garanin. *J. Phys. A: Math. Gen.*, 24, 1991.

[36] X. Hidalgo D. Garanin and E. Chudnovsky. *Phys. Rev. B*, 1998.

[37] E. Chudnovsky and J. Tejada. *Macroscopic Quantum Tunneling of the Magnetic Moment*. Cambridge University Press, 1998.

[38] E. M. Chudnovsky. *Phys. Rev. Lett.*, 46:8011, 1992.

[39] E. M. Chudnovsky and D. A. Garanin. *Phys. Rev. Lett.*, 79:4469, 1997.

[40] J. Villain H. Hartman-Bourtron R. Sessoli and A. Rettori. *Europhys. Lett.*, 27:159, 1994.

[41] N. Prokofév and P. Stamp. *Phys. Rev. Lett.*, 80:5794, 1998.

[42] C. Sangregorio T. Ohm and P. Paulsen. *Eur. Phys. J. B*, 6:195, 1998.

[43] C. Sangregorio T. Ohm and P. Paulsen. *J. Low Temp. Phys.*, 113:1141, 1998.

[44] C. Zenner. *Proc. Roy. Soc. London A*, 137:696, 1932.

[45] L. Gunther. *Europhys. Lett.*, 39:1, 1997.

[46] V. V. Dobrovitski and A. K. Zvezdin. *Europhys. Lett.*, 38:337, 1997.

[47] W. Wernsdorfer and R. Sessoli. *Science*, 284:133, 1999.

[48] M. McElfresh. *Fundamentals of Magnetism and Magnetic Measurements.* Quantum Design, Inc., 1994.

[49] R. Kubo and T. Toyabe. *Magnetic Resonance and Relaxation.* North-holland, Amsterdam, 1986.

[50] R. Kubo. *Hyperfine Interact.*, 8:731, 1981.

[51] Y. Uemura T. Yamazaki D. Harshman R. Nakai C. Huang. *Phys. Rev. Lett.*, 1980.

[52] R. Hayano Y. Uemura J. Imazato N. Nishida T. Yamazaki R. Kubo. *Phys. Rev. B*, 1979.

[53] Y. Uemura K. Nishiyama T. Yamazaki R. Nakai. *Solid State Commun.*, 1981.

[54] Y. J. Uemura T. Yamazaki D. R. Harshman M. Senba E. J. Ansaldo. *Phys. Rev. B*, 31:546, 1985.

[55] E. Fukushima and S. Roeder. *Experimental Pulse NMR: A Nuts and Bolts Approach.* Addison-Wesley, 1994.

[56] W. G. Clark M. E. Hanson F. Lefloch and P. Segransan. *Rev. Sci. Instrum.*, 66:2453, 1995.

[57] W. Wernsdorfer R. Sessoli A. Caneschi D. Gatteschi and A. Cornia. *Europhys. Lett.*, 50:552, 2000.

[58] P. Dalmas de Réotier and A. Yaouanc. *J. Phys.: Condens. Matter*, 9:9113, 1997.

[59] A. Keren. *Phys. Rev. B*, 50:10039, 1994.

[60] A. Lascialfari Z. Jang F. Borsa P. Carretta and D. Gatteschi. *Phys. Rev. Lett.*, 81:3773, 1998.

[61] A. Lascialfari D. Gatteschi F. Borsa A. Shastri Z. Jang and P. Carretta. *Phys. Rev. B*, 57:514, 1998.

[62] A. Lascialfari P. Carretta D. Gatteschi C. Sangregorio J. Lord and C. Scott. *Physica B*, 289.

[63] R. White. *Quantum Theory of Magnetism*. Springer-Verlag, second edition, 1983.

[64] Z. Salman A. Keren P. Mendels A. Scuiller and M. Verdaguer. *Physica B*, 106:289, 2000.

[65] Z. Salman A. Keren P. Mendels V. Marvaud A. Scuiller M. Verdaguer J. S. Lord and C. Baines. 2001.

[66] D. A. Garanin and E. M. Chudnovsky. *Phys. Rev. B*, 56:11102, 1997.

[67] A. Garg. *Phys. Rev. Lett.*, 81:1513, 1998.

[68] S. Miyashita and N. Nagaosa. *cond-mat/0108063*, 2001.

[69] N. Koloskova. In A. A. Manenkov and R. Orbach, editors, *Spin Lattice Relaxation in Ionic Solids*, page 232. Harper and Row, 1966.

[70] P. Politi F. Hartmann-Bourtron and J. Villain. *Int. J. Mod. Phys.*, 10:2577, 1996.

[71] B. Bleaney A. Abragam. *Electron Paramagnetic Resonance of Transition Ions*. Dover Publications: Mineola, 1986.

[72] J. S. Waugh and C. P. Slichter. *Phys. Rev. B*, 37:4337, 1988.

[73] J. S. Griffith. *The Theory of Transition-Metal Ions*. Cambridge University Press Publications: London, 1964.

[74] R. Giraud W. Wernsdorfer A. M. Tkachuk D. Mailly and B. Barbara. *Phys. Rev. B*, 87:57203, 2001.

[75] R. Giraud W. Wernsdorfer A. M. Tkachuk D. Mailly and B. Barbara. *cond-mat/0108133*, 2001.

μSR ו- NMR להבנת מינהור קוונטי של המגניטיזציה במולקולות בעלות ספין גבוה

זאהר סלמאן

μSR ו- NMR להבנת מינהור קוונטי של המגניטיזציה במולקולות בעלות ספין גבוה

חיבור על מחקר

לשם מילוי חלקי של הדרישות לקבלת תואר

דוקטור לפילוסופיה

זאהר סלמאן

הוגש לסנט הטכניון — מכון טכנולוגי לישראל

סיון תשס"ב חיפה מאי 2002

חיבור על מחקר נעשה בהדרכת דר' עמית קרן

בפקולטה לפיסיקה

הכרת תודה

הנני אסיר תודה לדר' עמית קרן על הדרכתו המסורה לאורך כל שלבי המחקר. תודה מיוחדת לפרופ' פיליפ מנדלס על שיחות ועצות מועילות ועל האירוח במעבדות לפיסיקת מצב מוצק, אוניברסיטת פריס-דרום. תודה מיוחדת לפרופ' מישיל וירדגיר ודר' ולרי מארבו על אספקת דגמים בנדיבות ועל שיחות פוריות.

תודה למשה ואבי על אספקת הליום סדירה, ותודה לשמואל ומרדכי על העזרה בבנית המערכת הנסיונית.

תודה לדר' יוחנה אדלר על תמיכתה ועזרתה בעניני מחשבים. תודה גם לחברי עמית קניגל ואדהם חשיבון על עזרתם ועל עצות מועילות. לאחי חנא, תאמר ואיאס, תודה.

אני אסיר תודה להורי לילא ומילאד על התמיכה והעזרה לאורך כל תקופת לימודיי.

אני מודה לטכניון, משרד המדע ותכנית שיתוף הפעולה צרפת-ישראל AFIRST על התמיכה הכספית הנדיבה בהשתלמותי

העבודה מוקדשת לפאולה

תוכן עניינים

רשימת איורים

רשימת טבלאות

תקציר

גודל יחידת זכרון מחשב נמצא בתהליך מתמשך של מיזעור כבר 40 שנה. כיום במחשבים וסרטים מגנטיים משתמשים ביחידות מגנטיות שמתנהגות באופן קלסי, ואשר שומרים על המגנטיזציה והמידע השמור בתוכם לאורך זמן. יציבות זו קיימת כתוצאה מהגודל של יחידות אלה והגודל של מחסום האנרגיה בין המצבים השונים של המגנטיזציה, העולה על $100\ k_B\mathrm{T}$ בטמפרטורת החדר. הגבול התחתון של גודל היחידה המגנטית, עבורו היחידה המגנטית מתנהגת בצורה קלסית, הנקרא "הגבול הקוונטי", הוא 10^2-10^5 ספינים ליחידה. מתחת לגבול זה תופעות קוונטיות יכולות לגרום לאיבוד המגנטיזציה השמורה ביחידת הזיכרון המגנטי. דוגמא לכך היא מולקולות בעלות ספין גבוה.

מולקולות בעלות ספין גבוה הן מולקולות המורכבות מיונים המצומדים ע"י אינטראקציה פרומגנטית או אנטיפרומגנטית; מולקולות אלה מסתדרות על שריג כאשר המרחק בין מולקולות שכנות גדול, כך שבטמפרטורות נמוכות (טמפרטורות הנמוכות מגודל האינטראקציה בין היונים J) המולקולות מתנהגות כמו ספינים גדולים בלי אינטראקציה ביניהם. כאשר למולקולה יש אנאיזוטרופיה מגנטית לאורך ציר z ניתן לכתוב את המילטוניאן הספין של מולקולה בודדת בצורה

$$\mathcal{H} = -DS_z^2$$

כאשר D הוא הפרמטר המתאר את גודל האנאיזוטרופיה ו- S_z הוא רכיב הספין של המולקולה בכיוון z. לכן האנריה של מצבי ספין מעלה $(+\hat{z})$ ומצבי ספין מטה $(-\hat{z})$ תהיה שווה. בטמפרטורות גבוהות (מעל לגודל האנאיזוטרופיה של המולקולה) הספין של המולקולה

יכול להתהפך ממצב מעלה למטה וההיפך ע"י מעבר טרמי מעל למחסום האנאיזוטרופיה, אבל כאשר הטמפרטורה נמוכה בהרבה ממחסום האנאיזוטרופיה, הערוץ היחיד האפשרי למעבר בין מצבי הספין הוא ע"י מינהור קוונטי. התנהגות זו מעניינת כי היא מאפשרת לנו "לראות" תופעות קוונטיות ע"י מדידות מאקרוסקופיות. תופעה זו נקראת מינהור קוונטי של המגנטיזציה.

מינהור בין מצבי ספין שונים אפשרי כאשר בהמילטוניאן של הספין מופיע ביטוי נוסף שאינו מתחלף עם רכיב הספין בכיוון ציר z, S_z. ביטוי זה יכול להיות אינטראקציה דיפולרית בין ספינים של מולקולות שכנות, אינטראקציה בין הספין הגרעיני לבין האלקטרוני במולקולות, ביטויים התלויים בחזקות גבוהות יותר של הספין המולקולרי הנגרמים משדה השריג, אינטראקציה של שדה הניצב לכיוון z עם הספין וכדומה.

בעבודה זו אנו מציגים מדידות המבוצעות בשלוש שיטות. מדידות מגנטיות באמצעות מגנטו-מטר, בהם ניתן למדוד את המגנטיזציה והסוסיפטביליות המגנטית כפונקציה של הטמפרטורה והשדה המגנטי, ממדידות אלה ניתן לחקור את התכונות המגנטיות הסטטיות של החומר הנלמד. את הדינמיקה של הספין המולקולרי ניתן לחקור ע"י מדידות רלקסצית/רוטצית ספין-שריג, המבוצעות באמצעות רלקסצית ספין של מיואון (μSR) או באמצעות מדידת תהודה מגנטית גרעינית (תמ"ג) של גרעיני מימן. במדידת רלקסצית ספין של מיואון משתילים מיואונים חיוביים מקוטבים בתוך הדגם הנמדד, ומודדים את הפולריזציה של המיואונים כפונקציה של הזמן, ואילו במדידת תמ"ג מכניסים את הדגם הנמדד לתוך שדה מגנטי גבוה כדי לקטב את הספינים הגרעיניים, וע"י הקרנת החומר בקרינת רדיו מודדים את הקיטוב של הספינים הגרעיניים.

בעבודה מוצגות תוצאות של מדידות רוטצית ספין של מיואון במולקולה האנאיזוטרופית Fe_8 בעלת ספין $S = 10$. בעזרת מדידות אלו מדדנו את השדה המגנטי המקומי שהמיואונים מרגישים כתוצאה מהספינים של מולקולות Fe_8 בסביבתם, תוצאות המדידות מעידות בבירור על קיום תופעת המינהור הקוונטי של המגנטיזציה במולקולות אלה.

מטרתנו העיקרית בעבודה זו היא לדעת איזה ביטוי בהמילטוניאן שולט בתופעה של

המינהור הקוונטי של המגניטיזציה במולקולות אנאיזוטרופיות, וזאת ע"י הבנה של הדינמי-קה של הספין המולקולרי במשפחה של מולקולות בעלות ספין גבוה, איזיטרופיות, שתכונותי-הן הפיסיקליות הן פשוטות יותר. מולקולות אלה הן $CrCu_6$, $CrNi_6$ ו- $CrMn_6$.

המגנטיזציה כפונקציה של השדה המגנטי בטמפרטורה $T = 2$ K הנמדדת בשלשת המולקולות האיזוטרופיות מראה התאמה לפונקצית ברילוין עם ערך רוויה בשדות גבוהים המתאים לספין $S = 9/2$ ב- $CrCu_6$, $S = 15/2$ ב- $CrNi_6$, ו- $S = 27/2$ ב- $CrMn_6$, מה שמעיד שהמולקולות אכן מיצרות מצבי יסוד עם ספין גבוה. את הסוסיפטביליות המגנטית של הנמדדת במולקולות כפונקציה של הטמפרטורה והשדה המגנטי ניתן לתאר באמצעות ההמילטוניאן

$$\mathcal{H} = -DS_z^2 - J\sum_{i=1}^{6} \vec{S}_0 \cdot \vec{S}_i - g\mu_B H_z S_z$$

כאשר $D \simeq 0$ הוא הפרמטר שמתאר את גודל האנאיזוטרופיה, $S_z = \sum_{i=0}^{6} S_i^z$ הוא רכיב הספין בכיוון z של כל המולקולה, H_z הוא השדה המגנטי בכיוון z, ו- J הוא גו-דל האינטראקציה המגנטית בין היונים בתוך המולקולה. $\vec{S}_0$ ו- $\vec{S}_i$ הם הספינים של יון ה-Cr ו- $Cu/Ni/Mn$ בהתאמה. מדידות אלה מראות שהתכונות המגנטיות הסטטיות ניתנות להסבר בצורה מלאה ע"י המודל הפשוט לפי ההמילטוניאן הנ"ל.

הקשר בין קצב דעיכת ספין-שריג $1/T_1$, הנמדד באמצעות μSR ותמ"ג, לבין הדינמיקה של הספין המולקולרי ניתן לבטא באמצעות

$$\frac{1}{T_1} = \frac{\gamma^2}{2}\int_{-\infty}^{\infty} dt\, \langle B_\perp(0) B_\perp(t)\rangle \exp(i\gamma H t)$$

כאשר γ הוא היחס הג'ירומגנטי של המיואון או הגרעין, $B_\perp$ הוא רכיב השדה המקומי הניצב לספין המיואון או הגרעין ו- H הוא השדה המגנטי החיצוני. באופן כללי ניתן לכתוב את קצב רלקסצית ספין-שריג בצורה

$$\frac{1}{T_1} = \frac{\Delta^2 \tau}{1 + \tau^2 \omega^2}$$

כאשר Δ הוא מידת גודל השדה המקומי המורגש ע"י המיואון או הגרעין, τ הוא זמן הקורלציה של השדה המקומי (או הספין המולקולרי) ו- $\omega \simeq g\mu_B H$.

המדידות מראות כי קצב דעיכת קיטוב הספין של מיואונים במולקולות עולה כאשר מורידים את הטמפרטורה. כאשר המולקולות נמצאות בשדה נמוך הקצב מגיע לרוויה בטמפרטורות נמוכות, לעומת זאת כאשר השדה המגנטי גבוה הקצב מגיע למקסימום וקטן בטמפרטורות נמוכות יותר.

קיטוב הספין של מיואון יכול לדעוך בתהליך דעיכת ספין-שריג, אולם תהליכים אחרים כמו יצירת מיואוניום יכולים גם לגרום לדעיכת קיטוב הספין. כדי לוודא שקיטוב הספין של המיואון אכן דועך בתהליך של דעיכת ספין-שריג אנחנו מבצעים מדידות של דעיכת ספין-שריג גם באמצעות תמ"ג. התוצאות של המדידות מראות שקצב דעיכת ספין-שריג הנמדד באמצעות מיואונים שווה לזה הנמדד באמצעות תמ"ג באותו שדה מגנטי, עד כדי קבוע כיול. עובדה זו מראה שאכן אנחנו מודדים את קצב דעיכת ספין-שריג באמצעות מיואונים, כמו כן רואים שקצב דעיכת ספין-שריג תלוי בשדה המגנטי החיצוני ולא תלוי בטכניקת המדידה.

חישוב של זמן הקורלציה של ספין-ספין מהערך של זמן דעיכת ספין-שריג, מראה שזמן זה בשדות נמוכים עולה כאשר מורידים את הטמפרטורה, ומגיע בטמפרטורות נמוכות לערך קבוע ובלתי תלוי בטמפרטורה. הערך של זמן הקורלציה במולקולות השונות שונה בכמה סדרי גודל בטמפרטורות גבוהות, אולם הוא בלתי תלוי בערך של הספין (או במולקולה עצמה) בטמפרטורות נמוכות.

ההתנהגות הנ"ל של זמן הקורלציה מראה שהדינמיקה של הספין של המולקולות האיזו-טרופיות נשלטת ע"י אינטראקצית ספין-פונון בטמפרטורות גבוהות, ואילו עבור טמפר-טורות נמוכות זמן הקורלציה נשלט בעיקר ע"י אינטראקציה שאינה תלויה בטמפרטורה ותלויה בצורה חלשה אם בכלל בערך של הספין המולקולרי, אינטראקציה זו היא כנראה האינטראקציה של הספינים הגרעיניים עם הספין המולקולרי.